Interaction of magnetic beads in microfluidic systems: fundamentals and applications

Dissertation

Frank Wittbracht

Bielefeld University

Department of Physics

Thin Films and Physics of Nanostructures

Declaration

I wrote this thesis by myself and used none but the indicated resources. Text and figures were partly taken from corresponding publications, which originate directly from this work.

Bielefeld, June 2012

Frank Wittbracht

Reviewers:

Prof. Dr. Andreas Hütten

Prof. Dr. Thomas Huser

Wer will, findet Wege,

wer nicht will, findet Gründe.

Table of contents

Publications and Conferences

Publications in peer-reviewed Journals:

1) A. Weddemann, F. Wittbracht, A. Auge, A. Hütten, *A hydrodynamic switch: Microfluidic separation system for magnetic beads*, Appl. Phys. Lett. **94** (17), 173501 (2009)

2) A. Auge, A. Weddemann, F. Wittbracht, A. Hütten, *Magnetic ratchet for biotechnological applications*, Appl. Phys. Lett. **94** (18), 183507 (2009) **Selected for publication in Vir. J. Nan. Sci. & Tech. 19 (21), 2009 and in Vir. J. Bio. Phys. Res. 17 (10), 2009**

3) A. Weddemann, F. Wittbracht, A. Auge, A. Hütten, *Positioning system for particles in microfluidic structures*, Microfluid. Nanofluid. **7** (6), 849 (2009)

4) A. Weddemann, B. Eickenberg, F. Wittbracht, A. Auge, A. Hütten, *A combined reaction separation lab-on-a-chip device for low Péclet number applications*, J. Appl. Phys. **106** (2), 024510 (2009) **Selected for publication in Vir. J. Bio. Phys. Res. 18 (3), 2009**

5) A. Weddemann, A. Auge, F. Wittbracht, D. Kappe, A. Hütten, *Dynamic simulations of the dipolar driven demagnetization process of magnetic multi-core nanoparticles*, J. Magn. Magn. Mat. **322** (6), 643 (2009)

6) A. Weddemann, A. Auge, F. Wittbracht, C. Albon, A. Hütten, *On the resolution limits of magnetic sensors for particle detection*, New J. Phys. **11**, 113027 (2009)

7) A. Weddemann, F. Wittbracht, A. Auge, A. Hütten, *Particle flow control by induced dipolar particle interactions*, Microfluid. Nanofluid. **10**, 459 (2010)

8) A. Weddemann, A. Auge, C. Albon, F. Wittbracht, A. Hütten, *Toward the magnetoresistive detecion of single nanoparticle: new strategies for particle detection by adjustment of sensor shape*, J. Appl. Phys. **107** (10), 104314 (2010) **Selected for publication in Vir. J. Nan. Sci. &Tech. 21 (23), 2010**

9) A. Auge, A. Weddemann, B. Vogel, F. Wittbracht, A. Hütten, *A level set based approach for modelling oxidation processes of ligand stabilized metallic nanoparticles*, Appl. Phys. Lett. **96** (9), 093111 (2010)

10) A. Weddemann, C. Albon, A. Auge, F. Wittbracht, P. Hedwig, D. Akemeier, K. Rott, D. Meissner, P. Jutzi, A. Hütten, *How to design magneto-based total analysis systems for biomedical applications*, Biosens. Bioelec. **26** (4), 1152 (2010)

11) A. Weddemann, F. Wittbracht, B. Eickenberg, A. Hütten, *Magnetic Field Induced Assembly of Highly Ordered Two-Dimensional Particle Arrays*, Langmuir **26** (24), 19225 (2010)

12) F. Wittbracht, B. Eickenberg, A. Weddemann, A. Hütten, *Towards a programmable microfluidic valve: Formation dynamics of two-dimensional magnetic bead arrays in transient magnetic fields*, J. Appl. Phys. **109** (11), 114503 (2011)

13) I. Ennen, C. Albon, A. Weddemann, A. Auge, P. Hedwig, F. Wittbracht, A. Regtmeier, D. Akemeier, A. Dreyer, M. Peter, P. Jutzi, J. Mattay, N. Mitzel, N. Mill, A. Hütten, *From Magnetic Nanoparticles to Magnetoresistive Biosensors*, Acta Physica Polonica A **121**, 420-426

14) F. Wittbracht, A. Weddemann, B. Eickenberg, M. Zahn, A. Hütten, *Enhanced fluid mixing and separation of magnetic bead agglomerates based on dipolar interaction in rotating magnetic fields*, Appl. Phys. Lett. **100** (12), 123507 (2012)
Selected for publication in Vir. J. Nan. Sci & Tech. 25(15), 2012

15) F. Wittbracht, A. Weddemann, B. Eickenberg, B. Riechers, M. Zahn, A. Hütten, *On the direct employment of dipolar particle interaction in microfluidic systems*, Microfluid. Nanofluid. DOI: 10.1007/s10404-012-0995-6

16) A. Regtmeier, F. Wittbracht, T. Rempel, A. Weddemann, A. Hütten, *Uniform growth of magnetic nanoparticles in a rotating magnetic field*, J. Nanopart. Res., **revision submitted**

Publications in Conference Proceedings:

1) A. Weddemann, A. Auge, F. Wittbracht, S. Herth, A. Hütten, *Interactions of magnetic particles in a rotational magnetic field*, Proceedings of the European COMSOL Conference 2008 in Hannover, ISBN 978-0-9766792-8-8

2) F. Wittbracht, A. Weddemann, A. Auge, A. Hütten, *Microfluidic separation system for magnetic beads*, Proceedings of the European COMSOL Conference 2008 in Hannover, ISBN 978-0-9766792-8-8

3) A. Auge, F. Wittbracht, A. Weddemann, A. Hütten, *Magnetic Ratchet*, Proceedings of the European COMSOL Conference 2008 in Hannover, ISBN 978-0-9766792-8-8

4) A. Weddemann, A. Auge, F. Wittbracht, C. Albon, A. Hütten, *Detection of Magnetic Particles by Magnetoresistive Sensors*, Proceedings of the third European COMSOL Conference 2009 in Milan, Italy, ISBN 978-0-9825697-2-6

5) A. Weddemann, A. Auge, F. Wittbracht, C. Albon, A. Hütten, *Dynamic Observation of Magnetic Particles in Continuous Flow Devices by Tunneling Magnetoresistance Sensors*, Proceedings of the third European COMSOL Conference 2009 in Milan, Italy, ISBN 978-0-9825697-2-6

6) F. Wittbracht, A. Weddemann, A. Auge, A. Hütten, *Fluid Flow Control by Magnetically Induced Dynamics of Particle Interactions*, Proceedings of the third European COMSOL Conference 2009 in Milan, Italy, ISBN 978-0-9825697-2-6

7) A. Auge, A. Weddemann, F. Wittbracht, B. Vogel, A. Hütten, *Oxidation of Metallic Nanoparticles*, Proceedings of the third European COMSOL Conference 2009 in Milan, Italy, ISBN 978-0-9825697-2-6

8) A. Weddemann, A. Auge, C. Albon, F. Wittbracht, A. Hütten: *Magnetoresistive Detection of Magnetic Beads and Nanoparticles—Spatial resolution and number resistive detection*, ICQNM 2010, Fourth International Conference on Quantum, Nano and Micro Technologies, St. Maarten, ISBN 978-1-4244-5807-3
Awarded with "Best Paper Award" in the Microtechnology Division

9) F. Wittbracht, A. Weddemann, A. Auge, A. Hütten: *Flow Guidance of Magnetic Particles by Dipolar Particle Interaction*, ICQNM 2010, Fourth International Conference on Quantum, Nano and Micro Technologies, St. Maarten, ISBN 978-1-4244-5807-3
Awarded with "Best Paper Award" in the Micro- and Nanofluidics Division

10) A. Regtmeier, F. Wittbracht, I. Dück, T. Rempel, A. Weddemann, A. Hütten, *A new route to control the enhancement of structural and*

anisotropy ordering in two-dimensional particle arrays, Nanotech Conference 2011, Boston

11) B. Eickenberg, F. Wittbracht, A. Weddemann, A. Hütten, *Microfluidic gate - Utilization of Self-Assembling, Free-Flowing Superstructures of Superparamagnetic Beads for Enhanced Mixing and Colloidal Separation*, ICQNM 2011, The Fifth International Conference on Quantum, Nano and Micro Technologies, Nice, France, ISBN 978-1-61208-151-9
Invited for publication in IARIA journal

12) F. Wittbracht, B. Eickenberg, A. Weddmann, A. Hütten, *Rotating magnetic field assisted formation of highly ordered two-dimensional magnetic bead arrays*, ICQNM 2011, The Fifth International Conference on Quantum, Nano and Micro Technologies, Nice, France, ISBN 978-1-61208-151-9

Oral presentations:

1) F. Wittbracht, A. Weddemann, A. Auge, A. Hütten, *Separation of magnetic beads by a combination of magnetic and hydrodynamic forces*, DPG Spring meeting 2009, Dresden

2) F. Wittbracht, A. Weddemann, A. Auge, A. Hütten, *Particle Flow Control by Magnetically Induced Dynamics of Particle Interactions*, European COMSOL Conference 2009, Milan

3) F. Wittbracht, A. Weddemann, A. Auge, A. Hütten: *Flow Guidance of Magnetic Particles by Dipolar Particle Interaction*, ICQNM 2010, Fourth International Conference on Quantum, Nano and Micro Technologies, St. Maarten

4) F. Wittbracht, A. Weddemann, B. Eickenberg, A. Hütten, *Assembly Of Highly Ordered Two-Dimensional Particle Arrays In Magnetic Fields For The Application In Microfluidic Devices*, The Second Conference on Advances in Microfluidics and Nanofluidics and Asian-Pacific International Symposium on Lab On Chip, Singapore, 2011

5) F. Wittbracht, A. Weddemann, B. Eickenberg, A. Hütten, *Magnetic nanoparticles as reconfigurable matter*, Young Researchers' Symposium FOR945, Bielefeld, 2011

6) F. Wittbracht, B. Eickenberg, A. Weddemann, A. Hütten, *Rotating magnetic field assisted microfluidics*, DPG spring meeting 2012, Berlin

Poster presentations:

1) F. Wittbracht, A. Weddemann, A. Hütten, *Microfluidic Separation System for Magnetic Beads*, DPG Spring meeting 2008, Berlin

2) F. Wittbracht, A. Weddemann, A. Auge, M. Panhorst, A. Hütten, *Microfluidic Separation System for Magnetic Beads*, CNT IX 2009, Frankfurt

3) F. Wittbracht, A. Weddemann, A. Auge, A. Hütten, *Microfluidic Separation System for Magnetic Beads*, European COMSOL Conference 2008, Hannover

4) F. Wittbracht, A. Weddemann, A. Auge, C. Albon, D. Akemeier, A. Hütten, *Control of particle flow in microfluidic systems by magnetically induced dipolar particle interactions*, Fourth Seeheim Conference on Magnetism 2010, Frankfurt

5) F. Wittbracht, B. Eickenberg, A. Weddemann, A. Hütten, *Rotating Magnetic Field Assisted Formation of Highly Ordered Two-Dimensional Magnetic Bead Arrays and Their Use in Microfluidic Systems*, Lab-On-a-Chip World Congress 2011, San Francisco

1   Introduction

The employment of magnetic particles and magnetic beads in microfluidic systems has been investigated extensively and led to the development of components in MEMS- and NEMS-devices (Gijs 2004, Pamme 2006; Niarchos 2003; Deng et al. 2001). Superparamagnetic microbeads are a vital component, since these composite objects, which consist of superparamagnetic nanoparticles embedded in a polymer matrix, combine properties of nano- and microscale systems (Haukanes and Kvam 1993). If subjected to on-chip or off-chip generated magnetic gradient fields, the magnetic content and, therefore, the magnetic particle may be manipulated (Weddemann et al. 2009; Weddemann et al. 2010 d; Panhorst et al. 2005; Brzeska et al. 2004, Auge et al. 2009). Usually, the generation of on-chip magnetic gradient fields involves lithography steps during the device fabrication.

However, the magnetic colloids themselves may be used to introduce a local magnetic gradient field on the microscale, which results from the inhomogeneous magnetic particle stray fields and may reduce the complexity of the microfluidic device. As extensively reported in the context of ferrofluids or magnetorheological liquids, the field contributions from the particles and the entailed magnetic interplay may strongly influence the fluid properties such as, e.g. viscosity or flow velocity (Shliomis and Morozov 1994; Love et al. 2005; Rosensweig 1996; Zahn and Pioch 1999; Moskowitz and Rosensweig 1967; Ginder et al. 1996; Ginder and Davis 1994). The coupling of the magnetic entities depends on the magnetic moment of the objects and on the concentration of the respective magnetic particles. In general, this means that the magnetic interplay needs only to be taken into account if a high concentration of magnetic particles is present within the suspension. For the strongly diluted case, low particle concentrations are present and the magnetic interplay can be omitted in the corresponding applications (Pamme and Manz 2003; Weddemann et al. 2009; Østergaard et al. 1999).
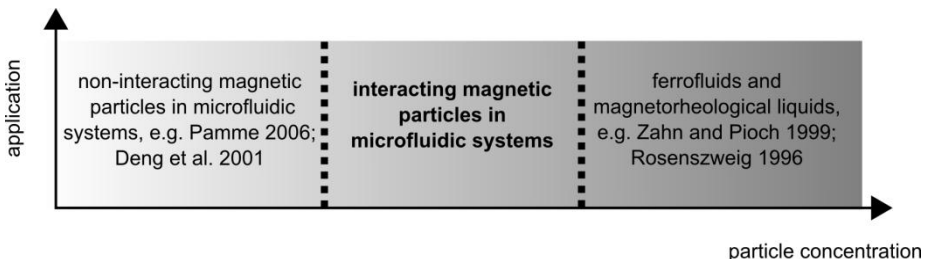

Fig. 1.1: Applications employing suspensions of magnetic particles in dependence on the particle concentration.

Between the extreme scenarios lies a regime of concentration which has only very recently attracted interest (figure 1.1) (Leunissen et al. 2009, Jäger and Klapp 2011; Jäger et al. 2012). The high concentration case can be modeled in the framework of continuum theories (Tang and Conrad 2000; Yeh and Chen 1997; Brigadnov and Dorfmann 2005), whereas the case of low concentrations needs to be described in the frame of discrete particle dynamics. The intermediate regime is governed by both types of scale behavior: mesoscale continuum fluid flow is superimposed by discrete particle motions (Laroze et al. 2008; Mørup et al. 2010; Kim and Park 2010; Derks et al. 2010; Karle et al. 2011 Lacharme et al. 2009).

Erickson et al. have developed on-demand configurable matter (Kalontarov et al. 2009) suspended in a carrier liquid, based on anisotropic porosity for hydrodynamic driven self-assembly. A comparable approach would be helpful for magneto-based microfluidics. Sawetzki et al. (2008) presented the employment of clusters of paramagnetic particles for mixing and flow guiding design. However, the cluster preparation is achieved by optical tweezers and, thus, difficult to be transferred to lab-on-a-chip systems. A possible realization of the concepts of on-demand assembly in a microfluidic device is presented in figure 1.2. The microvalve application presented in figure 1.2 shall not be scope of this work, but it illustrates the advantage of the employment of interacting superparamagnetic particles. Small isolated
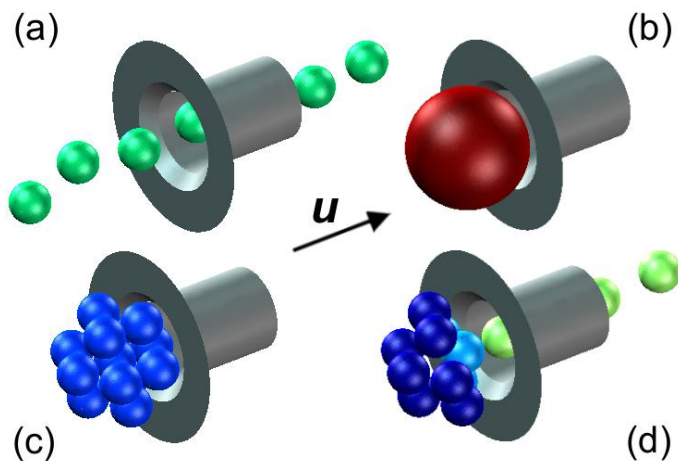
Fig. 1.2: Schematic representation of a microfluidic valve based on the on-demand assembly of superparamagnetic particles in the carrier fluid. (a) Small single particles may pass the constriction, whereas (b) large particles block the particle flow at the constriction of the channels irreversibly. (c) In contrast, on-demand assembled magnetic agglomerates may block the particle flow, but can also be disassembled if necessary by switching the magnetic field off.

particles may pass the constriction of the channel presented in figure 1.2(a), whereas larger particles block the particle flow due to interaction with topological features of the channel. However, the blocking of the flow with large particles is irreversible and, therefore, unfeasible in microfluidic applications. The interaction of magnetic particles, which have similar sizes as those in figure 1.2(a), may result in the formation of a magnetic agglomerate which allows to hinder the particle flow through the channel constriction (figure 1.2(c)). If superparamagnetic particles are employed, switching the magnetic field off, results in disassembly of the particle agglomerate (figure 1.2(d)) due to demagnetization of the particles. Applications based on these interactions employ particle suspension in the intermediate concentration regime, which allows to assign different functional tasks to the liquid itself.

The scope of this work is to increase the understanding of fundamental properties of the discrete dynamics in the intermediate concentration regime and to develop novel approaches to common challenges in microfluidics, e.g. mixing of self-assembly, based on these findings. A brief summary of the underlying phenomena and the governing equations of hydrodynamics and magnetism are given in chapter 2. Chapter 3 briefly describes the relevant experimental methods such as microfluidic channel fabrication, characterization and data evaluation. The fourth chapter summarizes the study on the formation dynamics and stability of dipolar coupled magnetic superstructures of different dimensionality. In chapter 5 two applications based on coupled magnetic superstructures are presented. Both involve homogeneous external magnetic fields, which allow for the perturbation of particle suspensions. However, the proposed microfluidic geometry presented in chapter 5.1 employs a static magnetic field, whereas the device operation of the microfluidic gate structure for simultaneous mixing and separation (chapter 5.2) is based on the employment of a rotating magnetic field. Despite the continuous flow applications presented in chapter 5, the dipolar coupling of magnetic particles may also be used for the generation of highly ordered two-dimensional hexagonal arrays, which may give rise to an efficient and fast method for surface patterning (chapter 6).

2 Theoretical background

In this chapter, important theoretical aspects of microfluidics as a special case of hydrodynamics and the basics of magnetism relevant for this thesis are summarized. We begin with hydrodynamic phenomena and afterwards discuss the relevant additional body force contributions to the (Navier-) Stokes equation.

2.1 A brief introduction to hydrodynamics with focus on the special case of microfluidics

In the field of hydrodynamics fluids are described, which consist of a larger number of discrete particles on the microscale $O(10^{23})$. To describe the state of the fluid exactly, complete knowledge of the particle positions and momentum would be essential. However, the large resulting number of degrees of freedom leads to the necessity of an effective theory, which reduces the problem of the large number of interacting discrete particles to the description of the fluid by the introduction of a small set of dependent variables. Additionally, an effective theory is also more suitable for the actual description of fluids, because usually the macroscopic behavior

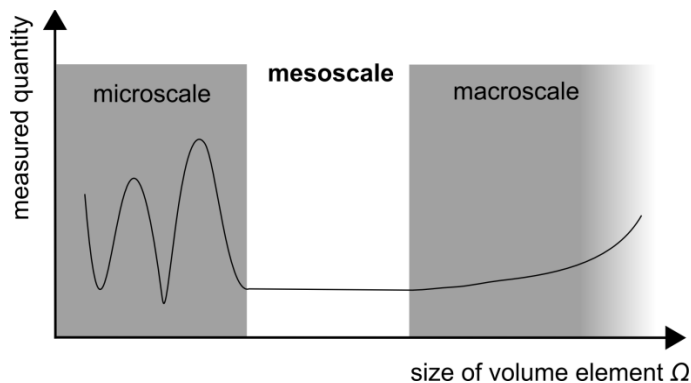**Fig. 2.1:** Sketch of the dependence of some measured quantity on the size of the volume element Ω. At the microscopic scale fluctuations occur due to the discrete structure of the system. A well-defined measurement may be obtained at the mesoscopic scale. Due to external forces a variation of the measured quantity at macroscopic volume elements is entailed; adopted from (Batchelor 2000).

of the fluid is of interest and no detailed information on the motion state of each contributing particle contained in the fluid is required. In this chapter, the validity of the *continuum hypothesis* may be assumed, which means that the fluid may be assumed to be perfectly continuous in structure without changing the macroscopic properties. In context with the continuum hypothesis, the concept of volume elements is introduced. A volume element has, in contrast to a point particle in classical mechanics, a finite size. If the size of the volume element was chosen to atomic dimensions, a measured quantity would show large fluctuations due to the discrete structure of the fluid as shown in figure 2.1. In order to reduce fluctuations, the volume element needs to increase in size. Once the number of atoms or molecules inside the volume element is sufficiently large, well-defined average values can be obtained. If the size of the volume element is chosen on a macroscopic scale, the measured quantity is averaged over a large number of atoms or molecules, but external influences may vary and the average may be taken over the region of interest. If the volume element of a liquid is chosen to be cubic with side length of ~ 10 nm, the number of atoms or molecules contained in the volume element is $\sim O\left(10^4\right)$. The size of such volume elements is large compared to the microscopic scale, but small compared to the macroscopic scale. In the following, volume elements of such mesoscopic dimensions may be assumed. If a certain liquid property at space point r is considered, strictly speaking the average of the liquid property over the volume element at space point r is meant. Additionally, to the continuum hypothesis states that along the described volume element, the system has reached thermal equilibrium in respect to the small set of space-dependent variables.

2.1.1 Effective parameters

The description of fluids in the framework of the continuum hypothesis allows to describe the effective behavior of a volume element by two fields. The *velocity* of a volume element is described by a vector field u, and the *pressure* inside the volume element is described by a scalar field p.

The reduction to an effective continuum theory entails that the interaction between discrete fluid particles needs to be described by material parameters, since the fluid elements are described as averages over a large number of molecules. In general, three parameters are sufficient to characterize the inner state, i.e. the microstructure of a fluid: the compressibility κ, the viscosity η, and the density ρ. The compressibility describes a relative change of volume when a fluid element is subjected to a pressure change and is defined as
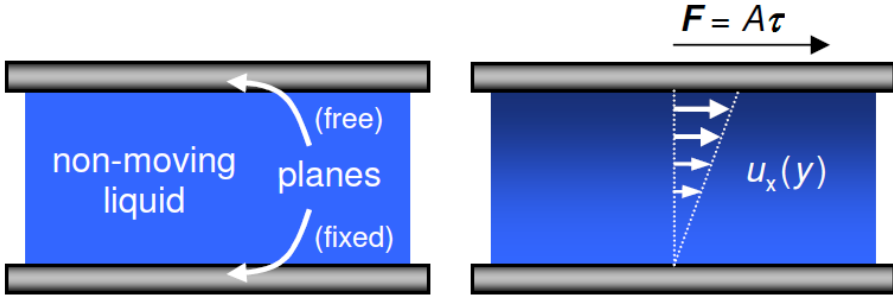
$$\kappa = \frac{1}{V}\frac{dV}{dp} \tag{2.1}$$

Fig. 2.2: Experimental setup employed in rheology measurements. The shear stress which results from the force $\boldsymbol{F}$ induces a fluid flow $\boldsymbol{u}$; reprinted from (Weddemann 2009).

where V and p denote the volume and the pressure, respectively. Compressibility values for liquids are usually very small compared to gases. In particular, the compressibility may be omitted if the flow velocities involved are very small compared to the speed of sound in the liquid. In the case of the microfluidic systems discussed in this work only liquids need to be described and the constraint of low flow velocities mentioned above is

met. Therefore, for the following $\kappa = 0$ may be assumed.
The density $\rho(\boldsymbol{r})$ represents a measure of the ratio of mass m and volume of a fluid element at a certain space point $\boldsymbol{r}$. The assumption of incompressible liquids allows to reduce the density to constant

$$\rho = \frac{m}{V} \quad . \tag{2.2}$$

The viscosity η describes the internal resistance to flow and is, therefore, a measure of the internal friction of a liquid. Experimentally, the viscosity can be measured in a simple setup which consists of two parallel plates with a liquid in between as presented schematically in figure 2.2. A *shear stress* $\tau = F/A$, where A is the surface area of the upper plate, is observed if a force $\boldsymbol{F}$ acts on the upper plate parallel to the plane, while the lower plate is kept stationary. The shear stress τ results in a fluid flow, which is parallel to the applied force and only dependent on the y-direction, which means that the velocity can be written as $\boldsymbol{u} = u_x(y)\boldsymbol{e}_x$. The derivative of $\boldsymbol{u}$ with respect to the y-direction is called the *strain rate* $\partial_y \boldsymbol{u}(y)$. In general, the shear stress is a function of the strain rate. The actual dependence of the shear stress on the strain rate differs for different liquids and is studied extensively in the field of *rheology*. A fluid is called *Newtonian* if the linear relation

$$\boldsymbol{\tau} = \eta \frac{\partial \boldsymbol{u}_x(y)}{\partial y} \tag{2.3}$$

is satisfied, where the constant η is the viscosity of the fluid. In this work, we will focus on *Newtonian* liquids, in our case, water or aqueous suspensions in general, which were used in all experiments. Examples of *non-Newtonian* fluids, which means that the assumption of a constant viscosity is not applicable, are blood, ketchup or modern paint which show a decrease of the viscosity with increasing shear rate. In contrast to blood, ketchup or paint, which are *shear thinning* materials, *shear thickening* fluids show an increase in the viscosity if the rate of shear increases. All material parameters introduced in this section are dependent on the temperature T. The viscosity of water, for example, decreases from $\eta_{\text{water}}(20°\text{C}) = 1.002$ mPa·s at $20°\text{C}$ to $\eta_{\text{water}}(80°\text{C}) = 0.355$ mPa·s at $80°\text{C}$ (Bruus 2008). However, all experiments presented in this thesis were performed at room temperature and we will, therefore, omit the temperature dependence of the material parameters in the following.

2.1.2 Conservation of mass and momentum

The first of the governing equations is the equation of continuity, which expresses the conservation of mass in classical mechanics. If we consider a fixed volume element Ω of arbitrary shape, we may write the total mass inside the domain as the volume integral over the density

$$M(\Omega,t) = \int_{\Omega} d\boldsymbol{r} \, \rho(\boldsymbol{r},t) \, . \tag{2.4}$$

In non-relativistic mechanics, $M(\Omega,t)$ can only change due to a mass flux through the surface $\partial\Omega$ of the domain Ω. Furthermore, we introduce the mass current density

$$\boldsymbol{J}(\boldsymbol{r},t) = \rho(\boldsymbol{r},t)\boldsymbol{u}(\boldsymbol{r},t) \tag{2.5}$$

which is given as the product of the density and the convection velocity $\boldsymbol{u}$. The time derivative of $M(\Omega,t)$ can be obtained by either the differentiation of the volume integral in (2.4) or the calculation of the surface integral of the mass current density through the surface $\partial\Omega$. Comparison of both results leads, together with *Gauss's theorem*, to the *equation of continuity*

$$\partial_t \rho = -\nabla \cdot (\rho \boldsymbol{u}) \, . \tag{2.6}$$

In the special case of an incompressible fluid, we may assume the mass density to be a constant material parameter independent of time and space as already mentioned above. As a result, the equation of continuity simplifies to

$$\nabla \cdot \boldsymbol{u} = 0 \,. \tag{2.7}$$

In order to obtain the second governing equation, the equation of motion for the velocity field $\boldsymbol{u}$, we may again consider a domain Ω, which is of arbitrary shape, but fixed and apply the conservation of momentum. The rate of change of the ith component of the total momentum inside Ω may be written as

$$\partial_t P_i(\Omega,t) = \partial_t \int_\Omega d\boldsymbol{r}\, \rho(\boldsymbol{r},t) u_i(\boldsymbol{r},t) = \int_\Omega d\boldsymbol{r}\left[(\partial_t \rho) u_i + \rho \partial_t u_i\right]. \tag{2.8}$$

The momentum $P_i(\Omega,t)$ is influenced by convection similar to the mass $M(\Omega,t)$ but $P_i(\Omega,t)$ also changes under the action of external forces according to Newton's second law. In general, we may distinguish contact forces from body forces. Whereas, the former act on the surface $\partial\Omega$ of Ω, e.g. pressure forces and viscosity forces, and the latter act on the volume of Ω, e.g. gravitational and magnetic forces. In summary, we may write the rate of change of the ith component of the total momentum inside Ω as

$$\begin{aligned}\partial_t P_i(\Omega,t) = &\, \partial_t P_i^{\mathrm{conv}}(\Omega,t) + \partial_t P_i^{\mathrm{press}}(\Omega,t) \\ &+ \partial_t P_i^{\mathrm{visc}}(\Omega,t) + \partial_t P_i^{\mathrm{body}}(\Omega,t)\end{aligned} \tag{2.9}$$

where the components $\partial_t P_i^{\mathrm{force}}$ denote the respective contributions due to contact and body forces. We will skip a detailed discussion of the contributions, which can be found in (Bruus 2008) and directly present the result for the general equation of motion of a viscous fluid in integral form

$$\int_\Omega d\boldsymbol{r}\left[(\partial_t \rho) u_i + \rho \partial_t u_i\right] = \int_{\partial\Omega} da\, n_j\left[-\rho u_i u_j - p\delta_{ij} + \sigma'_{ij}\right] + \int_\Omega d\boldsymbol{r}\, f_i \tag{2.10}$$

with $-n_i p\, da$ the ith component of the pressure force and the ith component of the viscous force $\sigma_{ij}'\, n_j\, da$, where σ_{ij}' denotes the viscous stress tensor. The contribution $f_i\, d\boldsymbol{r}$ describes an additional body force, which acts on the interior of Ω, e.g. a magnetic or gravitational force. By the combination of the pressure p and the viscous stress tensor σ' to the full stress tensor σ and under the assumption of a Newtonian fluid, which means that the internal friction due to shear stress and the internal friction due to compression show only small variations and may be assumed as

constants, and an incompressible liquid, we obtain the *Navier-Stokes equation* as the governing equation of motion

$$\rho\left[\partial_t \boldsymbol{u} + (\boldsymbol{u} \cdot \nabla)\boldsymbol{u}\right] = -\nabla p + \eta \nabla^2 \boldsymbol{u} + \boldsymbol{f} \ . \tag{2.11}$$

2.1.3 Microfluidics: a special case

The non-linear term in the Navier-Stokes equation makes the mathematical treatment of (2.11) complex and difficult. However, in the special case of microfluidics, where usually low flow velocities are present, the term may be omitted under certain circumstances. In order to determine the regime, where the non-linearity can be omitted, The Navier-Stokes equation can be recast in a dimensionless form by substitution of all physical variables in terms of characteristic scales. In particular, this reformulation of the Navier-Stokes equation allows to introduce one effective parameter, the so-called *Reynolds number*

$$Re \equiv \frac{\rho U L}{\eta} \tag{2.12}$$

with the characteristic velocity U and length scale L of the system. The dimensionless Reynolds number allows to estimate the relevant contributions in the Navier-Stokes equation. In the case of small Reynolds numbers, $Re \ll 1$, inertia effects play a minor role. This flow regime is often referred to as *creeping flow regime*. The time dependence of the solution can be omitted and the non-linear term vanishes, the linearized Stokes equation

$$\eta \nabla^2 \boldsymbol{u} = \nabla p \tag{2.13}$$

is obtained. In the special case of microfluidic devices, the characteristic velocities are usually on a scale of $U = O(10^{-4} \text{ m/s})$ and the geometrical features have characteristic length scales $L = O(10^{-4} \text{ m})$. If we assume the density and viscosity to be $\rho = O(10^3 \text{ kg/m}^3)$ and $\eta = O(10^{-3} \text{ Pa·s})$, which corresponds to water at room temperature, we obtain $Re = O(10^{-2}) \ll 1$. Therefore, in the special case of microfluidics, inertia effects may be omitted and the fluid flow is described by the linearized Stokes equation (2.13), which may be solved analytically if highly symmetric problems are considered. One of the most famous examples is the *Poiseuille flow* through a cylindrical tube of length L with the radius R. Under the assumption of a pressure difference Δp between the tube entrance and exit, the solution for the flow profile results with 'no-slip'-condition to the parabolic profile
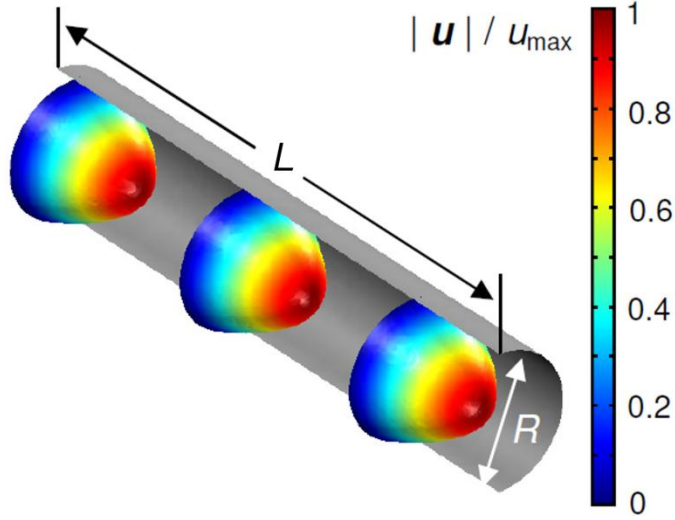
Fig. 2.3: Poiseuille flow through a pipe,which results from a pressure difference Δp between the inlet and outlet, reprinted from (Weddemann, 2010).

$$u(r) = \frac{\Delta p}{4\eta L}\left(R^2 - r^2\right).$$ (2.14)

Figure 2.3 shows a representation of the flow profile. A similar result can be found if two parallel plates are considered. In the case of the microfluidic channels that will be presented in this thesis, where the fluid flow results from a pressure difference of the inlet and outlet reservoirs, neither (2.14) nor the result for parallel plates, describe the flow profile exactly. The actual resulting flow profile has to be calculated by numerical methods, e.g. *finite element methods* (FEM). Nevertheless, the general properties of the flow profiles obtained will still be comparable to the *Poiseuille flow* which means that the velocity of the boundary layer of the fluid at the channel walls will vanish ('no-slip'-condition) and the shape will be comparable to the profile obtained from (2.14).

2.1.4 Diffusion and related problems

In addition to the steady time-independent flow solutions obtained from the linearized Stokes equation (2.13), the time-dependent phenomena of diffusion need to be discussed. The important equations for diffusion can be derived from two fundamental assumptions: (1) a substance moves down its concentration gradient and (2) the conservation of mass is satisfied. The material flux J depends on the concentration gradient dc/dx if we restrict the discussion to a one-dimensional problem. We obtain *Fick's first law*

$$J = -D\frac{\partial c}{\partial x} \tag{2.15}$$

There is a linear relation between the material flux and the concentration gradient. The constant D is called the *diffusivity* of the substance. We obtain a change in the concentration $c(x)$ within a small one-dimensional (liquid) element of length dx where the material flux into dx and out of dx differs as a direct consequence of the assumption of conservation of mass. Therefore, we may conclude for the difference of the material fluxes with respect to the region dx in the time interval Δt that

$$\big(J(x+dx) - J(x)\big)\Delta t = -\Delta c \cdot dx . \tag{2.16}$$

By rearrangement of (2.16) and conversion to derivatives, we find

$$\frac{\partial c}{\partial t} = -\frac{\partial J}{\partial x} \tag{2.17}$$

which can be combined with (2.15) and results in Fick's second law, the *diffusion equation*, if D may be assumed to be constant,

$$\frac{\partial c}{\partial t} = D\frac{\partial^2 c}{\partial x^2} . \tag{2.18}$$

The diffusion equation can also be derived for the three-dimensional case analogous to the discussion above, see e.g. (Jackson 2006). Based on the diffusion equation, the time evolution of a concentration distribution can be calculated. In the following, two specific examples will be analyzed: (1) the diffusion from a point source and (2) the diffusion across an interface. In order to calculate the one-dimensional diffusion from a point source, we define the initial concentration distribution with the Dirac delta function as $c(x, t = 0) = c_0\delta(x)$. The solution of (2.18) to this initial condition is given by the Gaussian distribution

$$c(x,t) = \frac{c_0}{\sqrt{4\pi D t}} e^{-x^2/(4Dt)} . \tag{2.19}$$

In the context of microfluidic systems, the diffusion across an interface is a more common problem, which needs to be addresses. Experimentally, this can be realized by filling a tube with a solution from the one side and water from the other side as schematically presented in figure 2.4.
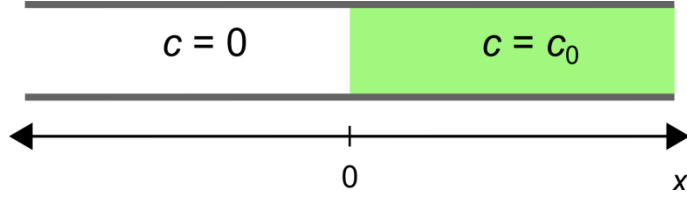
Fig. 2.4: Schematic representation of a tube filled with two fluids with analyte concentrations $c = 0$ and $c = c_0$. The interface at $x = 0$ separates the different concentration regimes. As time evolves intermixing results solely from the diffusion of the analyte species towards the lower concentrated phase according to (2.22) if no convective flux is present.

After filling the tube, the concentration is $c = c_0$ for $x > 0$ and $c = 0$ for $x < 0$, if we choose the interface of the liquid as the origin and we assume the filling of the tube to occur without intermixing of two solvents. In order to solve the diffusion equation with the initial condition described above, the region with $c = c_0$ can be described as an infinite row of infinitesimal point sources. Each of those point sources individually shows an evolution of the concentration according to (2.19). The solution to the problem of diffusion across an interface is then the superposition of the point source solutions, since the diffusion of a solute from one of the point sources occurs independently of the solute concentration which spreads from the other point sources. The linearity of this behavior directly results from the first fundamental assumption which already led to (2.15). Therefore, the concentration distribution can be written as

$$c(x) = \frac{c_0}{\sqrt{4\pi Dt}} \int_{x'=0}^{\infty} dx' \, e^{-(x'-x)^2/(4Dt)} \tag{2.20}$$

with x' the center of a point source and dx' the respective distance between adjacent point sources. With the complementary error function

$$\text{erfc}(z) = \frac{2}{\sqrt{\pi}} \int_{x}^{\infty} dy \, e^{-y^2} \tag{2.21}$$

the results for the concentration distribution in (2.20) can be written as

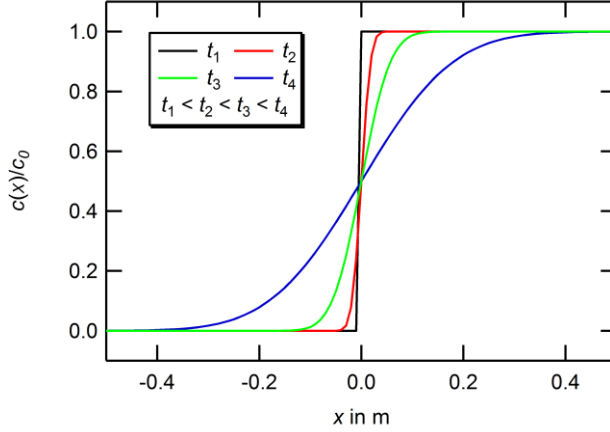$$c(x) = \frac{c_0}{2} \, \text{erfc}\left(-\frac{x}{\sqrt{4Dt}} \right) . \tag{2.22}$$

Fig. 2.5: Time evolution of the concentration distribution according to (2.22). The diffusivity was chosen to $D = 1\ \mathrm{m^2/s}$.

The result for the time evolution of $c(x)$ is plotted in figure 2.5 for a diffusivity of $D = 1\ \mathrm{m^2/s}$ and times $t_1 = 10^{-6}\ \mathrm{s}$, $t_2 = 10^{-4}\ \mathrm{s}$, $t_3 = 10^{-3}\ \mathrm{s}$, $t_4 = 10^{-2}\ \mathrm{s}$. In particular, we find that the slope at $x = 0$ reduces in steepness as time evolves. The result for the diffusion across an interface (2.22) will be used in section 5.2 to allow to estimate the mixing efficiency of the microfluidic gate structure.

2.1.5   Spherical objects in a liquid

For small spherical objects, which are dissolved in a liquid, the forces exerted on the particles are either induced by the fluid flow or arise from external sources. Examples for the external forces are gravity and buoyancy, but also magnetic contributions which will be discussed in section 2.2 in more detail. For the sake of simplicity, all external force contributions will be summarized in $\boldsymbol{F}_{\mathrm{ext}}$ in the following. The transfer of momentum towards the particles can only be calculated if the flow itself is known. As explained in section 2.1.3, there is usually no analytical solution to the velocity profile and, consequently, the momentum transfer to the particles needs to be evaluated by numerical methods. However, in the case of very small Reynolds numbers ($Re \ll 1$), *Stokes drag law*

$$\boldsymbol{F}_{\mathrm{drag}} = 6\pi\eta\, R_{\mathrm{hyd}}(\boldsymbol{v} - \boldsymbol{u}) \tag{2.23}$$

applies if a sphere with hydrodynamic radius R_{hyd} moves at the speed $\boldsymbol{v}$ in a flow $\boldsymbol{u}$. If very small particles are considered, inertia effects may be omitted and the particle velocity $\boldsymbol{v}$ instantaneously equals the flow velocity of the surrounding liquid $\boldsymbol{u}$. If the particle diameter is assumed to be small compared to the geometrical size scale L, the

particle can be described as a point mass of density ρ_{part} and Newton's second law may be applies to calculate the behavior of the particle. The particle velocity is then given by (Warnke 2003)

$$\boldsymbol{v} = \boldsymbol{u} + \frac{\boldsymbol{F}_{\text{ext}}}{6\pi\eta\,R_{\text{hyd}}} \tag{2.24}$$

if in addition to the momentum transfer from the flow, external forces influence the particles. In the special case of a spherical object in a liquid, the diffusivity is given by

$$D = \frac{k_B T}{6\pi\eta R_{\text{hyd}}} \tag{2.25}$$

where k_B and T denote Boltzmann's constant and the temperature, respectively. The relation (2.25) was derived by Einstein (1906) in his work on the explanation of Brownian motion.

2.2 Superparamagnetic beads and dipolar interaction

For magnetic-based microfluidic applications, superparamagnetic particles are mainly used. A schematic representation of a superparamagnetic bead is shown in figure 2.6. These usually micron-sized spherical objects consist of three main components: (1) nanometer-sized superparamagnetic particles embedded in a (2) polymer matrix, which is encoated in a (3) functional ligand shell allowing for the optional specific of non-specific binding of additional components to the particle surface (molecules, DNA strands, cells etc.). The magnetic moment of the microbeads can be adjusted by external field contributions and demagnetization on short time scales can be achieved once the perturbation is switched off again (Weddemann et al. 2010 c). At room temperature the magnetic state of free superparamagnetic particles is governed by thermal contributions which exceed the inner anisotropy energy. Such interplay results in a rapid fluctuation of the orientation direction of the magnetic moment, where orientation changes occur on smaller time scales than the minimum measurement times. Consequently, a free superparamagnetic particle resembles a virtually non-magnetic characteristic. If the particle is brought into a magnetic field, a resulting torque leads to the alignment of moment vector and field axis which reduces the fluctuation and entails an effective magnetic moment $\boldsymbol{m}$. If a spherical homogeneously magnetized particle is
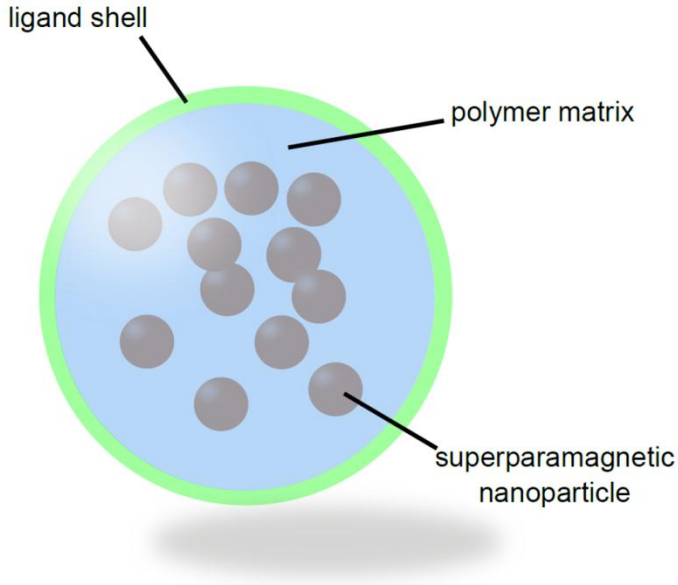
Fig. 2.6: Schematic representation of a superparamagnetic bead.

considered, the external magnetic field $\boldsymbol{H}$ is given by the dipolar expression (Jackson 1975)

$$\boldsymbol{H}(\boldsymbol{r}) = \frac{1}{4\pi}\left(\frac{3\langle\boldsymbol{m},\boldsymbol{r}\rangle\boldsymbol{r}}{r^5} - \frac{\boldsymbol{m}}{r^3}\right) \tag{2.26}$$

where $\langle\bullet,\bullet\rangle$ denotes the Euclidian inner product.

The force which acts on a particle with magnetic moment $\boldsymbol{m}$ exposed to an external magnetic field $\boldsymbol{H}_{\text{ext}}$ is given by (Zborowski et al. 1999)

$$\boldsymbol{F} = \mu_0(\boldsymbol{m}\cdot\nabla)\boldsymbol{H}_{\text{ext}} \tag{2.27}$$

with μ_0 the permeability of the vacuum. In particular, no resulting forces can be reported if an isolated magnetic object is placed in a homogeneous magnetic field. Employing rotating magnetic fields introduces additional effects due to shear stresses, which may act on particle agglomerates as presented in chapter 4. A first estimation of the governing physical driving force can be obtained from calculation of the dimensionless *Mason number*

$$Mn = \frac{16\eta\omega}{\mu_0\chi^2 H^2} \tag{2.28}$$

20

by comparison of typical scales of hydrodynamic and magnetic contributions, where η is the viscosity of the fluid surrounding the particles, ω the angular velocity of the magnetic field, χ the effective dimensionless susceptibility of the beads and $\boldsymbol{H}$ denotes the field strength. The Mason number was originally introduced in a different form for the study of electrorheological fluids under shear (Gast and Zukoski 1989). Different definitions of the Mason number can be found in the literature (Melle et al. 2003; Bosis et al. 2002). We will employ the definition of the Mason number (2.28) given by Petousis et al. (2007).

3 Experimental methods

This chapter describes the experimental methods employed to fabricate and characterize microfluidic structures. Additionally, the techniques for the generation of external magnetic fields are presented. Furthermore, methods for the evaluation of experimental data are discussed.

3.1 Fabrication of microfluidic channel structures

All microfluidic channel structures in this thesis were fabricated by the employment of standard soft-lithography methods of polydimethylsiloxane (PDMS) as vastly described in the literature (Friend and Yeo 2010; Ng et al. 2002). The general fabrication steps can be summarized as shown in the flow chart in figure 3.1. In the following, the employed fabrication steps for the microfluidic systems used in this work are described.

In our experiments, we use classic choice of PDMS which is Dow Corning's Sylgard 184 Kit. This is a two component kit which contains a curing agent and the base polymer. The cross-linker and elastomer are mixed in a mass ratio of 1:5. The rigidity of the PDMS can be reduced by an increase of the base polymer contribution. As shown in figure 3.1, the first step during the channel fabrication is to draw and fabricate a mask in order to use it afterwards for the structuring of a mold. The masks used in this work were all prepared by optical laser lithography: a glass slide is covered with a positive photo resist which can be patterned using a light source and a developer bath. After patterning, the glass slide with the residual resist is covered with a thin metal film (usual thickness about 100 nm) by magnetron sputtering. The metal film can be removed along with the residual resist from the glass substrate in a remover bath. A more detailed description of the laser lithography process which includes all relevant process parameters can be found in (Wittbracht 2009).

3.1.1 Mold fabrication

The molds are fabricated by optical lithography of the negative photo resist SU-8 3025 (Microchem) on previously cleaned silicon wafers. In a clean room, the silicon substrates are coated with the negative photo resist in a spin-coater. The thickness dependence on the spin-coating parameters of the resist can be obtained from the

manufacturer. Afterwards, the photo resist needs to pass through three heating cycles in a furnace:

(1) *soft-bake*: 65°C for 5 min, 95°C for 15 min, cool to room temperature
(2) *post-exposure bake*: 65°C for 5 min, 95°C for 5 min, cool to room temperature
(3) *hard-bake*: 160°C for 15 min, cool down to room temperature

As the name of the second heating step already suggests, the exposure is performed after the soft-bake. The exposure of the SU-8 3025 to the ultraviolet light from the lithography system (Thermo Oriel) and the following post-exposure bake lead to an increased chemical stability of the exposed portions of the resist. Therefore, in the following development step, the unexposed regions of the resist can be washed away with the developer solution mr-dev 600 (Microresist). Finally, the hard-bake further increases the mechanical stability of the mold and allows to reliably reuse the mold after casting the PDMS.
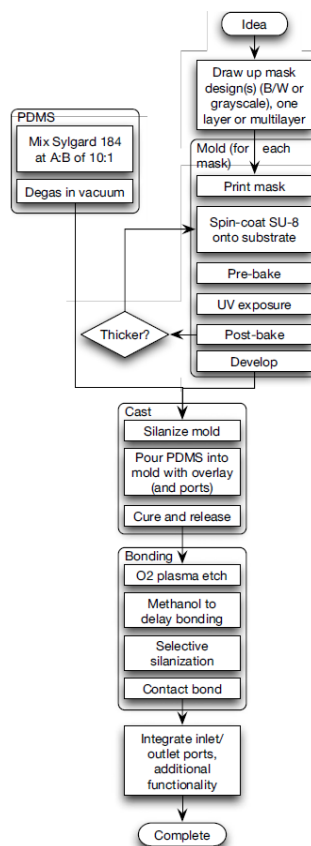

Fig. 3.1: Soft-lithography fabrication process for microfluidic channels. (Reprinted with permission from Friend and Yeo 2010. Copyright 2010, American Institute of Physics)

3.1.2 Casting, curing, cutting and bonding

For casting, the two components of PDMS are thoroughly mixed and degassed. Afterwards, the PDMS mixture is poured onto the mold and a curing procedure is performed. In our case, curing is obtained from heating the PDMS-covered mold to 80°C for 4 hours. Finally, the PDMS may be peeled off the mold and cut according to the designated geometry which includes inlet and outlet reservoirs.

After the release and cutting of the PDMS structure, the obtained microfluidic channels need to be sealed. In addition, the surface of the fabricated PDMS will be hydrophobic, which is unfavorable for the designated microfluidic application, since water-based suspensions of magnetic beads are employed. The plasma oxidation of the PDMS allows for both reducing the hydrophobicity and bonding of the PDMS to a substrate. Plasma bonding entails the formation of covalent bonds between two plasma treated surfaces; in our case, the PDMS channel structures and a previously cleaned silicon wafer terminated with silicon oxide. Details on the method of plasma treatment and the plasma chamber that was used can be found in (Hellmich 2006).

3.2 Optical microscope

Experiments are recorded with the digital optical microscope shown in figure 3.2. The commercially available microscopy system Keyence VHX-600 is equipped with a CCD camera and allows for different magnifications by the employment of zoom objectives. For the experiment presented in this thesis, the VH-Z100UR objective is

Fig. 3.2: Optical microscope Keyence VHX-600 with VH-Z100UR zoom objective.

used. This setup allows to observe magnetic micro beads with a maximal spatial resolution of about 0.375 µm at a maximum frame rate of 28 frames per second (fps). The adjustable stand of the microscope together with the pivotable stage allows for a simple integration of the magnetic field setups presented in the following section.

3.3   External magnetic fields

Basically, two different types of magnetic field setups are used throughout the experiments: (1) a coil setup for the generation of a homogeneous magnetic field with static orientation and (2) a magnetic stirrer for the generation of a rotating magnetic field.

3.3.1   Coil setup

The coil setup which is used for the experiments presented in chapter 5.1 is shown in figure 3.3. It consists of two electromagnetic coils with a rectangular cross-section, which are mounted onto a coil frame. Together with an iron core, this coil setup allows to generate a homogeneous magnetic field at a field strength of 490 Oe at the sample position between the opposing pole pieces. In order to change the relative orientation of the microfluidic channel structure and the external magnetic field, the sample is mounted onto the stage of the optical microscope, which can be rotated.

Fig. 3.3: Image of the coil setup for magnetic field generation

3.3.2   Magnetic stirrer

The rotating magnetic fields employed in the experiments presented in the chapters 4, 5.2, and 6 are generated by a commercially available magnetic stirrer (RCT basic, IKA GmbH, Germany) as often employed in chemistry laboratories to accelerate chemical reactions. In contrast to the usual application, no macroscopic magnetic stir bar is present in the experiments, but the magnetic micro particles in the bead solution are subjected to the field generated by a mechanically rotated permanent magnet. The magnetic stirrer setup shown in figure 3.4 may be used in a frequency regime between 50 rpm and 1500 rpm. However, due to stability of the rotation movement, preliminary experiments have revealed that the frequency regime between 50 rpm and 900 rpm is feasible for experiments due to the occurrence of mechnical vibrations at the sample position if higher rotation frequencies are employed. The variation of the magnetic field strengths is limited to the use of different permanent magnets in the stirrer setup. Two different stirrers are equipped

Fig. 3.4: Image of the magnetic stirrer setup.

26

with two different permanent magnets, which result in a maximum field strength of 330 Oe and 690 Oe at the sample position. According to video microscopy results of low concentrated bead solutions under the influence of the static magnetic fields generated by the permanent magnets, the magnetic field gradient at the sample position does not result in a particle movement if the sample is positioned in the centre of the stirrer setup. Therefore, we may omit the gradient of the magnetic field and assume the magnetic field to be homogeneous at the sample position.

3.4   Data evaluation

In all experiments presented in this thesis, microscopy data are recorded with the Keyence VHX-600. Based on the microscopy images or the video footage, further analysis of the data is required. Basically, three different aspects need to be addressed: (1) in the experiments which are performed in microchannel structures (chapter 5), the movement of particles or superstructures has been monitored. In the following, we will refer to this as particle tracking, regardless, if isolated particles or superstructures are of interest. In all studies the (2) counting of particles, agglomerates or objects in general needs to be achieved and, in particular, in the context of surface patterning as presented in chapter 6 the investigation of the (3) structural properties of agglomerates will be addressed.

Manual particle tracking is performed with the free software ImageJ (Rasband 1997-2011) and the MtrackJ plugin (Meijering et al. 2012). In order to count particles, two methods are feasible: (a) manual counting of individual particles and (b) counting of
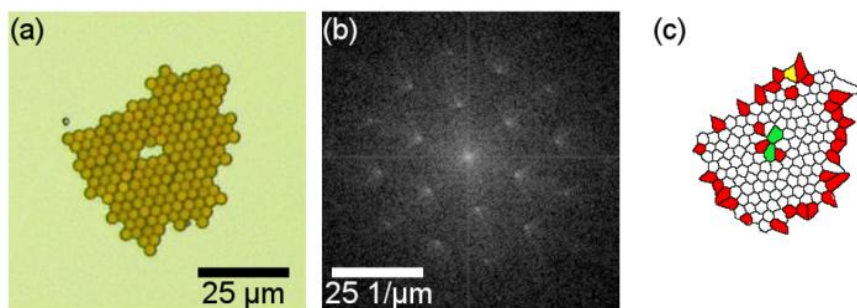

Fig. 3.5: Optical microscopy image of a highly ordered two-dimensional assembly under the influence of a magnetic field rotating at 400 rpm (a). The FFT of (a) shows the hexagonal symmetry of the assemblies and the high degree of ordering (b). (c) Voronoi tessellation of (a) where cells with 4-, 5-, 6- and 7-fold symmetry are dyed in yellow, red, white and green, respectively.

particles based on the number of pixels within a specified area at a defined color value. In comparison with the manual counting, the pixel-based counting of particles entails an error of about 2.4%, which can be attributed to fluctuation of contrast within the microscopy images. The structural properties of resulting agglomerates are evaluated by manual counting in the case of vacancies (zero-dimensional defect structures) and grain boundaries (one-dimensional defects). Grains are defined as regions with unbroken hexagonal symmetry. Furthermore, the structural properties of larger grains can also be identified with fast Fourier transforms (FFT) of the microscopy images. The FFT can be performed with ImageJ. An example of a microscopy image of an agglomerate and the corresponding FFT of the image is presented in figure 3.5(a) and figure 3.5(b), respectively.

As can be seen in the FFT image, we can directly identify the hexagonal ordering of the clusters. Additional information on the structural properties can be obtained from the Voronoi tessellation of figure 3.5(a) which is presented in figure 3.5(c). Voronoi cells with 4, 5, 6 and 7 neighbors are dyed in yellow, red, white and green, respectively. The Voronoi tessellation also shows the high degree of hexagonal ordering inside the clusters, but additionally reproduces the frustration along the edge and around the two vacancies in the middle of the cluster.

3.5 Magnetic beads

All superparamagnetic beads employed in this work are commercially available and were purchased from Invitrogen Dynal. In dependence on the actual experimental conditions either Dynabeads® MyOne™, Dynabeads® M-270 or Dynabeads® M-280 were used. The beads are suspended in adequate solution. In case of the Dynabeads® M-270 SA (streptavidin functionalization), the carrier liquid is, e.g. PBS buffer solution. Datasheets and manuals for the suspensions of these spherical beads can be obtained from the manufacturer. Some characteristics of the employed microparticles

Table 1: Characteristics of the magnetic beads used in this work according to Fonnum et al. (2005). CV denotes the standard deviation of the bead diameter distribution in percentage of the mean bead diameter.

Bead	Diameter (µm)	CV (%)	ρ (g/cm^3)	Iron (mg/g)
MyOne™	1.05	1.9	1.7	255
M-270	2.80	< 3	n.a.	n.a.
M-280	2.83	1.4	1.4	118

are summarized in table 1. In particular, the small standard deviations of the size distributions are important for experiments, which involve ordering of particles. As vastly described in literature, particle size distributions with small standard deviations are beneficial for the ordering of particle assemblies (Ennen 2008; Sudfeld 2005; Korgel et al. 1998; Motte et al. 2005; Ohara et al. 1995) and, therefore, the standard deviations of the particle size distributions also influence the magnetic field induced assembly.

4 Stability and formation dynamics of dipolar coupled superstructures

In order to develop functional components with the ability to assemble on-demand, it is essential to understand their fundamental properties and the underlying formation dynamics. The investigation of microscaled systems allows to understand the magnetic force contributions relevant for the formation, since the size and time scales of these systems allow for the dynamic observation by optical microscopy.

As described in section 2.2, no magnetic force is obtained if an isolated magnetic particle is placed in a homogeneous magnetic field. However, for sufficiently high particle concentrations, the interaction becomes increasingly important and may result in agglomeration of contiguous magnetic objects as schematically summarized in figure 4.1. If the distance between two particles is not too high, the alignment of their magnetic moment vectors entails an attractive force which leads to the formation of one-dimensional chain structures (figure 4.1(a – c)). The chain direction is parallel to the field axis as long as viscous drag forces are small enough to be omitted. The chain orientation follows the field vector if changes are carried out adiabatically (figure 4.1(d)). The chain rotation is damped by the viscosity of the carrier liquid which exerts shear forces along the chain and leads to a phase lag which results in a mismatch of the chain direction and magnetic field orientation if rotational magnetic fields are considered. If the angular field velocities exceed a critical limit, stresses surpass the breaking point of the chain and such rod structures
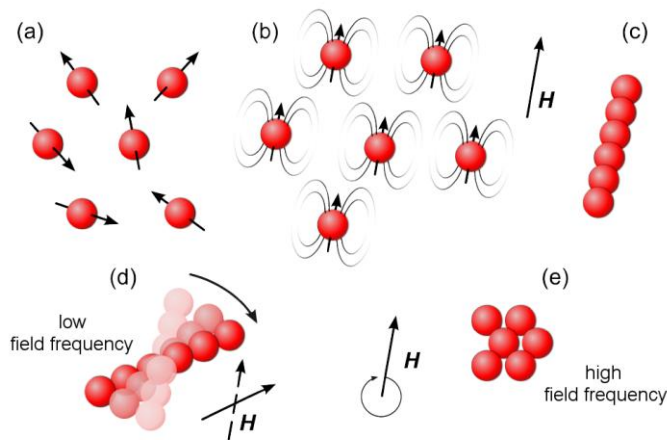

Fig. 4.1: Schematic representation of the magnetic field induced assembly of magnetic particles for different configurations of the external magnetic field.

cannot maintain their stability. As described in this chapter, chain breakage is followed by reorganization of particles in highly ordered two-dimensional sheets (figure 4.1(e)). The results presented in this chapter originate from a project which was experimentally realized together with Bernhard Eickenberg and have been published in (Wittbracht et al. 2011) and (Wittbracht et al. 2012 b).

4.1 One dimensional agglomerates

The fundamental behavior and stability of one-dimensional magnetic agglomerates have been investigated by numerous research groups. As can already be concluded from (2.28), the properties of these combined objects strongly depend on the external magnetic field and, therefore, most studies focus on the stability behavior in dependence of the field characteristics. We immediately learn from equations (2.26) and (2.27) that the magnetic moments involved determine the magnetic force. Under the assumption that all other related parameters are fixed, an increase in the magnetic force can be found, if the magnetic moment is increased. Consequently, the chain stability is enhanced, if larger magnetic moments are present. This relation was directly proven in the force spectroscopy experiments of Furst and Gast (1999). They employed dual-trap optical tweezers to determine rupture forces of particle chains parallel and perpendicular to the applied magnetic field direction. The analysis of the micromechanics of dipolar particle chains was realized with 0.85 μm polystyrene beads with embedded mono-domain iron-oxide particles. Typical rupture forces of particle chains as determined by Furst and Gast lie in the range of 6.4 pN to 45 pN depending on the strength of the dipoles. The influence of a rotating magnetic field on paramagnetic particle chains was investigated by Vuppu et al. (2003) by video microscopy of rotating chains immersed in a carrier liquid. Up to a critical rotation frequency, the angular velocities of chain and field rotations were identical. A further increase of the field frequency resulted in chain breakage due to the viscous drag forces parallel to the chain axis and reordering of the chain fragments is obtained. In particular, they were able to show the existence of an S-shaped dislocation of particles in the assembly in the frequency transition regime. At such frequencies, magnetic cohesion and viscous shear forces are on the same scale. Such S-dislocated states were further investigated by Petousis et al. (2007) who characterized the chain breaking event in dependence on the Mason number and lengths of individual chains. Within their works, they developed a discrete theoretical model and were able to conclude that the maximum number of particles in a stable chain is proportional to $Mn^{-1/2}$. In the following, our experimental findings on the formation of superstructures and the transient dynamics will be presented.

For the experimental realization, commercially available superparamagnetic Dynabeads M-280 streptavidin are employed (Fonnum et al 2005). These beads have
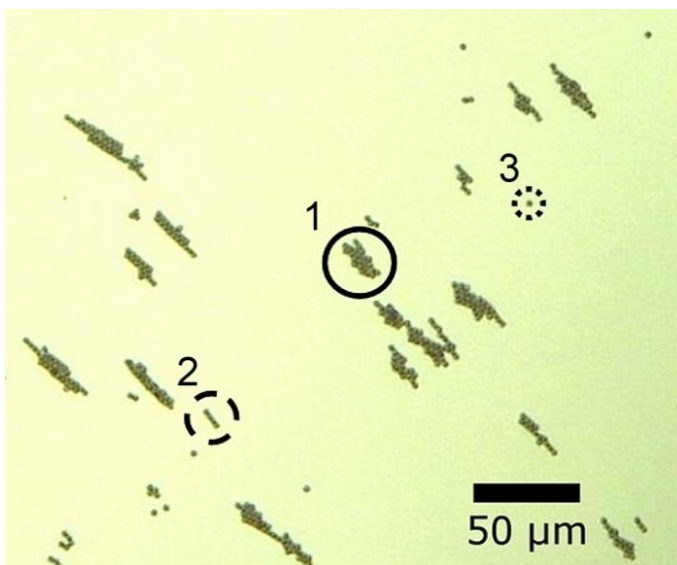
Fig. 4.2: Optical microscopy image of the magnetic bead assemblies during field rotation. Two-dimensional particle arrays (continuous) can be distinguished from bead chains (dashed) and individual particles (dotted).

a mean diameter of 2.8 μm with a standard deviation of 1.4% of the mean bead diameter and are delivered at a concentration of 10 mg/ml. Three dilutions of the bead solution at concentrations of 83 μg/ml, 100 μg/ml and 125 μg/ml are prepared. The rotating magnetic field is realized by the magnetic stirrer setup as described in section 3.3.2 with a magnetic field strength of 330 Oe at the sample position. According to the data obtained by Fonnum et al. (2005), for the applied magnetic field strength, the bead magnetization exhibits a linear response. At the beginning of the experiment, a 1 μl droplet of the bead solution is deposited on top of a silicon wafer which is situated in the centre of the magnetic stirrer hotplate. During the spotting procedure, the field direction is kept stationary which results in the assembly of particles within chain structures. After 3 minutes, the field is set into rotation with different frequencies and microscopy images are collected at fixed time steps.

Exemplarily, a typical microscopy image of magnetic bead assemblies in a rotating magnetic field is shown in figure 4.2. Three different classes of objects can be distinguished: (1) two-dimensional particle arrays/clusters (2) bead chains with high aspect ratio consisting of more than 4 beads (3) individual beads and small agglomerates which consist of a maximum of up to 4 beads. The separation between the classes (2) and (3) is chosen to match the expectation value of superstructures prepared without a magnetic field as we will see in chapter 6.

We start the analysis of the dynamics by focusing on the evolution of the mean chain length in respect to various experimental parameters. The dependence of the
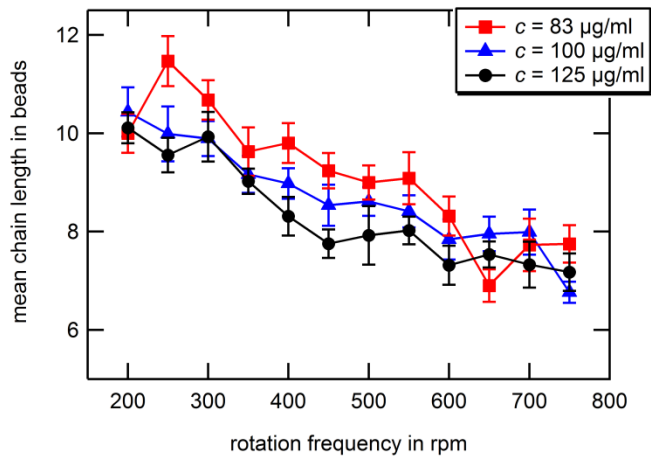
Fig. 4.3: The mean chain length decreases with increasing rotation frequency of the applied external magnetic field and with increasing particle concentration.

mean chain length on the rotation frequency of the magnetic field and the particle concentration is shown in figure 4.3. Corresponding microscopy images are presented exemplarily in figure 4.4. The micrographs show characteristic particle structures for 200 rpm, 500 rpm, and 750 rpm. The samples only contain a small degree of isolated beads but the formation of two- dimensional clusters was not initiated. In particular, transitional objects can be identified as exemplarily presented in the upper right corner of figure 4.3(a). The S-shaped chain agglomerate results from the interaction of the chain with the surrounding carrier liquid. Similar objects are also reported by Petousis et al. (2007) and Melle et al. (2003).

The results presented in figure 4.3 are obtained from the evaluation of microscopy images taken 15 s after the initiation of the magnetic stirrer rotation. At
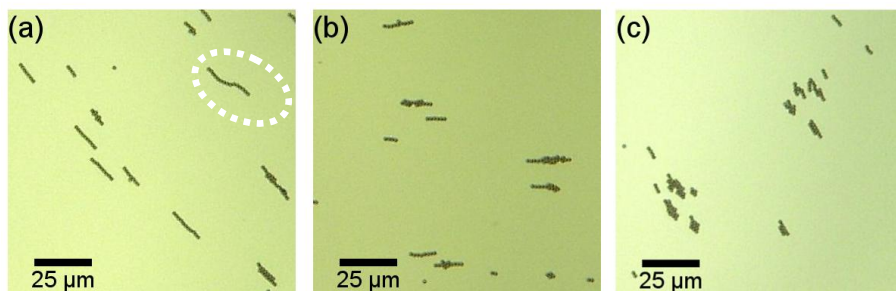

Fig. 4.4: Optical microscopy images in (a), (b) and (c) show characteristic chains for rotation frequencies of 200 rpm, 500 rpm and 750 rpm, respectively. In the upper right corner of (a) a transitional S-shaped chain object can be observed.
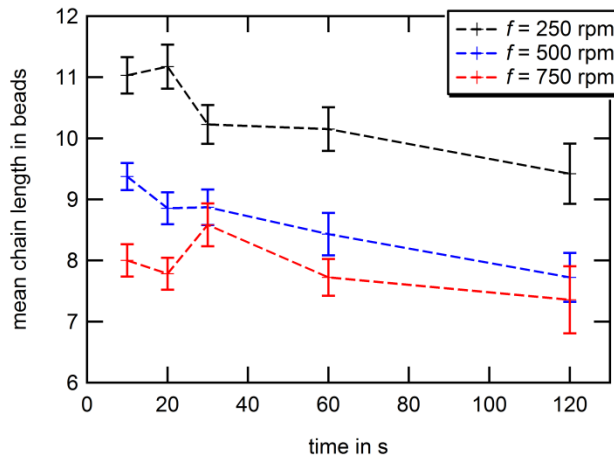
Fig. 4.5: The mean chain length decreases with increasing time. For high rotation frequencies of the magnetic field, a rapid decay of the mean chain length can be observed.

the chosen time, a high concentration of bead chains is obtained. With increasing field rotation frequency, a decreasing mean chain length for all investigated concentrations can be reported.

Qualitatively, the frequency dependence of the mean chain length is in good agreement with the experimental work of Vuppu et al. (2003) who already reported a slow decrease of the chain length with increasing rotation frequency of the external field in the range between 200 and 450 rpm. In comparison to the theoretical results by Petousis et al. (2007), we can conclude that we also obtained a decrease in the stable chain lengths with increasing rotation frequency of the external magnetic field. Surprisingly, a higher bead concentration also entails lower mean chain lengths. Qualitatively, this effect can be understood equivalently to the nucleation dynamics according to the LaMer model (LaMer and Dinegar 1950) for nanoparticle fabrication: In a first step, particle nuclei are formed if the local concentration exceeds a critical concentration threshold. The higher the concentration, the more nuclei are formed during this process. With monomers forming nuclei, the monomer concentration falls below the critical threshold and no additional nucleation processes take place. Instead, the remaining free monomers contribute to the growth of particles. If the monomer concentration is equally distributed along the sample, larger particles are obtained the less particle nuclei are formed in the previous step. Therefore, high initial concentrations may result in a high number of small particles while a small number of large clusters can be obtained via employment of a low concentration of monomers. This mechanism corresponds to the magnetic bead chain formation if we replace the monomers by the magnetic beads and the particle nuclei

by small one-dimensional assemblies: For high bead concentrations, a high degree of small chains are formed due to the higher probability of initial cluster formation.

However, variations for the different concentrations are in the range of 1 to 2 beads in length only. Therefore, we may average over the concentrations for further data series. If we assume the growth of clusters to be governed by the addition of bead chains to a two-dimensional cluster, the details about the microscopic process remain uncertain. However, the evolution of the mean chain length with time may lead to further understanding of the dynamics involved. The time-dependence of the chain lengths for different rotation frequencies is presented in figure 4.5. The mean chain length decreases with increasing time for every set of data presented. Furthermore, a descending order of the mean chain length with increasing rotation frequencies is found, which corresponds to the findings displayed in figure 4.3 and discussed above. At this point, it is not clarified whether the chains as a whole or partially attach to clusters, because both processes may lead to a reduction of the mean chain length with increasing time.

4.2   Two-dimensional agglomerates

In order to analyze the formation and growth mechanism of two-dimensional magnetic bead arrays, the time-dependence of the object ratio is evaluated. The results are shown in figure 4.6. No significant time dependence of the object ratio for free particles is obtained, whereas the ratio of objects classified as chains and clusters
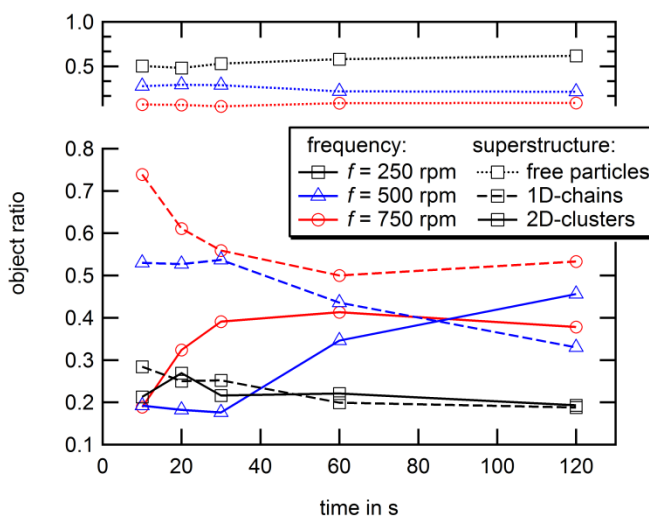

Fig. 4.6: Object ratio in respect to time for rotation frequencies of 250 rpm (black), 500 rpm (blue) and 750 rpm (red) classified according to the object superstructure.

decreases and increases with time, respectively. The growth of two-dimensional bead arrays is governed by the addition of chains to previously formed clusters. The time dependence of the object ratio may also be used as an indication for the microscopic processes involved in the cluster formation: At a rotation frequency of 750 rpm, we obtain a saturation value for the ratio of bead chains which can be found in the solution after approximately 60 s. If we assume that bead chains attach as a whole, the chain ratio would decrease with time and no saturation value would be found. Therefore, we may conclude, that both processes are involved: During the cluster growth, chains are not only attached as a whole but also partially. The time-dependent behavior of the mean cluster area is presented in figure 4.7(a) which shows an increase of the cluster size with time. The experimental observations reveal a mean cluster size of about 20 particles after less than 10 s of exposure at low frequencies and concentrations. At higher rotation frequencies, larger clusters are formed due to the reduced chain stability and, consequently, a higher probability of chain addition to previously formed agglomeration seeds. In particular, the adjustment of field frequency and bead concentration in the solvent allows to control the cluster size after a certain exposure time which will define the working regime of future devices.

In order to quantify the growth dynamics in more detail, we introduce the bead ratio

$$c_{\text{bead}} = \frac{N_{\text{obj}}(t)}{N_{\text{all}}(t)} \tag{4.1}$$

with $N_{\text{obj}}(t)$ the time-dependent number of beads within a certain object class and $N_{\text{all}}(t)$ the overall number of beads within the sample. The evaluation of c_{bead} for different object classes and rotation frequencies is presented in figure 4.7(b). Clusters grow at the cost of chains while the ratio of individual beads and small agglomerations shows variations on the scale of statistical fluctuations. They are randomly dispersed along the sample and have no further magnetic beads nearby to interact with and, therefore, do not form larger assemblies.

Since the concentration of individual beads can be assumed to be time-independent, the transition from individual beads to chain-like agglomerates can be omitted for the cluster formation dynamics. Therefore, only the transition from chain-like agglomerates to clusters has to be taken into account for the time-dependent formation dynamics. The formation of clusters resembles the case of a first order reaction comparable to deposition of monomers during the growth of nanoparticles (Sugimoto 2001), therefore, we may conclude that the decay of the concentration of particles in chain structures c_{chain} can be assumed to be proportional to the concentration itself. Hence, the cluster growth follows the exponential law
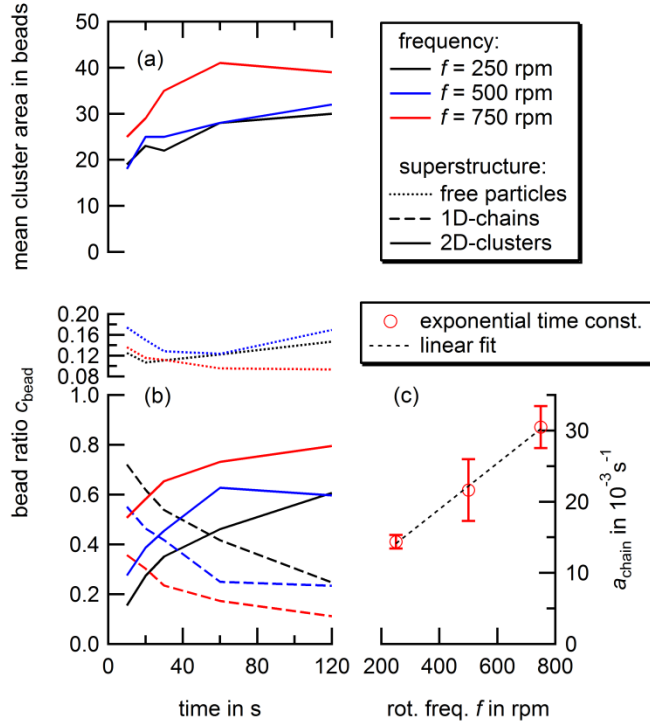
Fig. 4.7: Cluster growth dynamics. (a) The mean cluster area increases in respect to time and depends on the rotation frequency of the magnetic field. (b) Evolution of the object concentrations c_{bead} for confinements of different dimensions. (c) Time constant a_{chain} obtained from exponential fits to the experimental data represented in subplot (b).

$$c_{\text{bead}}^{\text{cluster}} = 1 - \exp\left(-a_{\text{chain}}(f)t\right) \tag{4.2}$$

with $a_{\text{chain}}(f)$ the frequency dependent chain dissociation rate. In general, the chain dissociation rate would be expected to be dependent on the Mason number (2.28), but as only the rotation frequency of the magnetic field is changed in the experiments, we will limit the analysis to the frequency dependence of a_{chain} which can be obtained from the data presented in figure 4.7(b) if the data points are fitted according to equation (4.2). This simple model is in very good agreement with the experimental observations. In particular, this approach allows to estimate the frequency dependence of a_{chain}. As shown in figure 4.7(c), a linear relation, $a_{\text{chain}} \sim f$, is in strong agreement with the obtained experimental data along the analyzed frequency regime. This behavior can be understood in the frame of a very simple model: Due to the regarded length scales, the Reynolds number of the system satisfies $Re \ll 1$, and, consequently, the stresses which act along the chain are governed by Stokes friction. Therefore, the fluid exhibits forces that are linear in the chain velocity which itself is

linear in the chain rotation frequency and the chain length and, consequently, an increase of frequency results in a linear increase of chain lengths that will no longer maintain their stability. For the frequencies discussed, this behavior can be seen in figure 4.3. In the case of a wider regime of frequencies, this is no longer true, but the maximum chain length decreases $\sim Mn^{-1/2}$ and consequently, if only the frequency dependence is studied $\sim f^{-1/2}$ according to Petousis et al. (2007). Our results are in the range of Mason numbers between 0.001 for 250 rpm and 0.0025 for 750 rpm according to the magnetic data for M-280 beads presented by Fonnum et al. (2005). In this Mason number regime, Petousis et al. obtained a Mason number dependent decrease of the chain stability, which can be approximated linearly. In the case of a wider Mason number regime, the above stated proportionality to $Mn^{-1/2}$ is reported due to additional instability phenomena, which originate from the increasing phase lag of rotating chains as the field rotation frequency is increased. The obtained results for the frequency dependent chain dissociation rate and mean size of one- and two-dimensional objects allow to adjust the experimental parameters for specific microfluidic applications based rotating magnetic fields.

To conclude, we have investigated the formation of two-dimensional magnetic bead arrays under the influence of a rotating magnetic field. The growth process dynamics of bead clusters is governed by the addition of bead chains to previously formed agglomeration seeds and may be characterized as a first order reaction. Since the formation dynamics are described by exponential laws in respect to time, large clusters can already be observed after short exposure times. This particular finding supports the applicability of such agglomerations as switchable microfluidic components triggered by an external magnetic field. According to our findings, it should be possible to realize switching times down to 10 s, however, with various parameters free to adjust the cluster properties to specific needs, the setup may be further optimized in this regard. In particular, we found the rotation frequency to be linearly connected to the time constant for the assembly of cluster-like objects which could be related to the increasing forces on bead chains with increasing rotation frequencies due to Stokes friction for the frequency regime up to several 100 rpm. Therefore, the results show the trend to obtain even higher cluster formation rates at higher field frequencies. The choice of a suitable rotation frequency will be of great importance for the design of microfluidic applications involving micro bead arrays, e.g. programmable valves. Concerning such applications, future experiments need to be carried out in order to analyze the stability of assembled clusters against fluid flow induced shear stresses and transitions between open and closed states.

5   Direct employment of dipolar coupling in microfluidic devices

In chapter 4 the fundamental behavior with respect to formation dynamics and stability of dipolar coupled superstructures which consist of superparamagnetic beads are analyzed. In dependence of the dimensionality of the particle agglomerates various applications are possible. Since the dimensionality strongly depends on the applied magnetic field properties, applications for different external magnetic field configurations are presented. The results are also published in (Weddeman et al. 2011), (Wittbracht et al. 2012 a) and (Wittbracht et al. 2012 b)

5.1   Employing a static magnetic field for the control of particle flow in microfluidic devices

This section focuses on the possibility to use the dipolar coupling of particles in diluted magnetic particle suspensions in order to achieve a controlled particle flow. As already discussed in chapter 4, the formation of chain-like agglomerates occurs on small time scales and stability of these objects is maintained if shear stresses do not surpass critical values. Therefore, the flow of particle agglomerates may be controlled via the relative orientation of the microfluidic channels and the external homogeneous magnetic field. Since a macroscopic magnetic field can be used for the flow control, no magnetic components on the microscale are necessary for the operation of the proposed microfluidic device.

   In order to discuss the operation principle of the proposed microfluidic geometry a schematic representation of the main components is presented in figure 5.1. A reservoir of circular shape is connected to a rectangular channel (figure 5.1(a)). If a pressure difference between the inlet and outlet is assumed, the expected flow profile at the junction, is obtained from (2.13) via finite element simulations and depicted in figure 5.1(b). The simulations were performed by Alexander Weddemann. When immersed in a homogeneous magnetic field H the magnetic moments of diluted particles within the microfluidic structure aligns with the external field direction. If the particle concentration is sufficiently high, adjacent particles interact with the stray fields of neighboring particles, which results in an attractive force. As a result, the dipolar coupling of the particles entails a self-assembly process as presented in figure 5.1(c). The movement of sufficiently long chains is determined by the angle between the chain axis and the fluid flow direction. For large angles, the chains are blocked at the junction area due to interaction with the reservoir wall. Chains below a
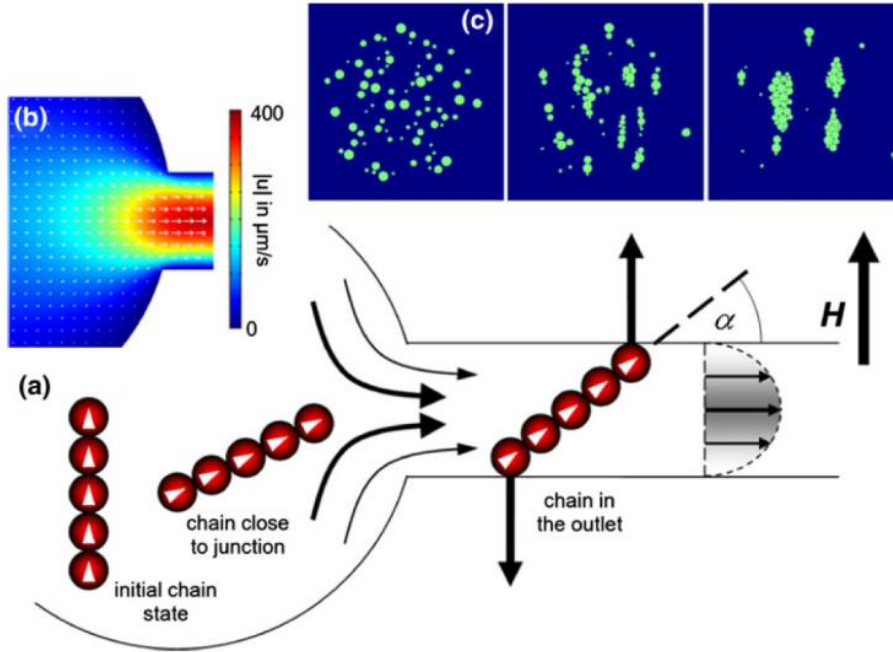
Fig. 5.1: Schematic representation of the key components of the proposed microfluidic device. (a) Reservoir channel junction: the orientation of particle superstructures can be controlled by the external magnetic field direction and determines the movement. The hydrodynamic torque which results from the flow profile (b) has to be considered in addition to the magnetic torque. (c) Finite element simulation results show the self-assembly process of neighboring magnetic particles due to their stray fields.

critical length may enter the channel, but their migration can be limited by the magnetic torque which is entailed by a mismatch of the external field direction and the flow direction through the channel. Based on the previous discussion of the reservoir-channel junction, an extended device, which employs the presented guiding strategy for particles, is shown in figure 5.2(a). This programmable reaction chamber consists of two inlet channels I_B and I_D and two outlet channels *drain* and *waste*, which are connected to the reaction site R. Alignment of the magnetic field direction parallel to the orientation B or D results in a particle flow from the respective inlet channels to the reaction site R. The particle flow can be blocked, if the magnetic field direction is changed, as already discussed above.

The optical microscopy image in figure 5.2(b) shows the PDMS channel structure (upper) and a cross section of the SU-8 mold (lower). The 2 mm long channels have a width of 30 µm and a height of 25 µm. Dimensions of the semiaxes' of the elliptical reaction site were chosen to 160 µm and 90 µm. During operation of the microfluidic device, the channel structures are positioned on the pivotable sample
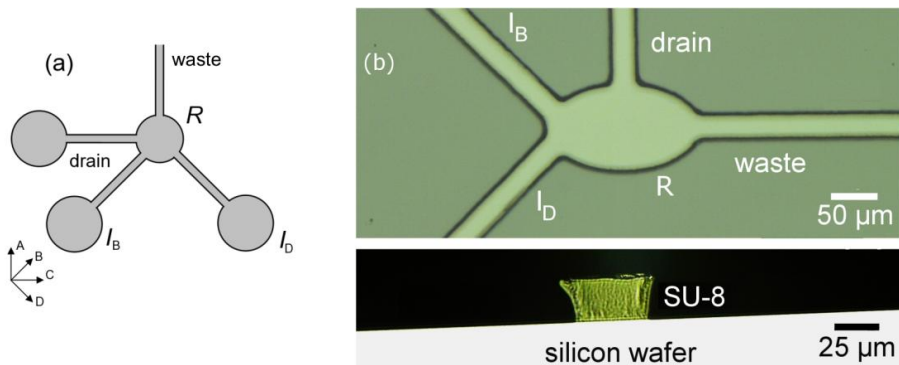
Fig. 5.2: (a) Schematic representation of the microfluidic device for particle flow control. (b) Optical microscopy image of the PDMS channels (upper) and a cross section of the SU-8 mold (lower).

holder of the Keyence VHX-600 (3.2) between the pole pieces of the coil setup described in 3.3.1.

The reservoirs I_B and I_D are filled with 1 µl droplets of suspensions of Dynabeads® MyOne™ and Dynabeads® M-280. The different sizes of the particles allow to distinguish between particle species which enter the reaction site from different reservoirs. Particle concentrations of 10 mg/ml are applied in both cases. The sequence of optical microscopy images in figure 5.3 shows a typical fill/drain process. To ease the particle tracking M-280 beads are highlighted in red and MyOne™ beads are highlighted in blue. No particle flow to the reaction site can be observed, if the magnetic field direction is not aligned with the microfluidic channels. Rotating the magnetic field towards direction D results in a flow of magnetic superstructures from inlet I_D towards the reaction chamber (figure 5.3(a-b)). The flow velocity during the filling process is about 100 µm/s. No flow of MyOne™ beads to the reaction site can be found, if the direction of the magnetic field is kept parallel to the channel which is connected to the inlet I_D. By field rotation towards direction B, the flow from inlet I_D to the reaction chamber is inhibited and simultaneously a flow of particles from I_B to the reaction site can be found (figure 5.3(c-e)). Similar to the situation presented in figure 5.3(a), flux of particles from channel directions which do not coincide with the magnetic field direction is inhibited. As the MyOne™ bead chain enters the reaction chamber R, the stray field interaction between the two agglomerates within R entails merging to a new superstructure composed of both bead species (figure 5.3(f)). As the magnetic field rotates towards direction A, the newly composed superstructure breaks apart due to interactions with the walls of the reaction site (figure 5.3(g)). Alignment of the field with direction A enables the flow of the large fragment of the superstructure to the drain channel (figure 5.3(h-i)), while the small chain fragment remains in the reaction
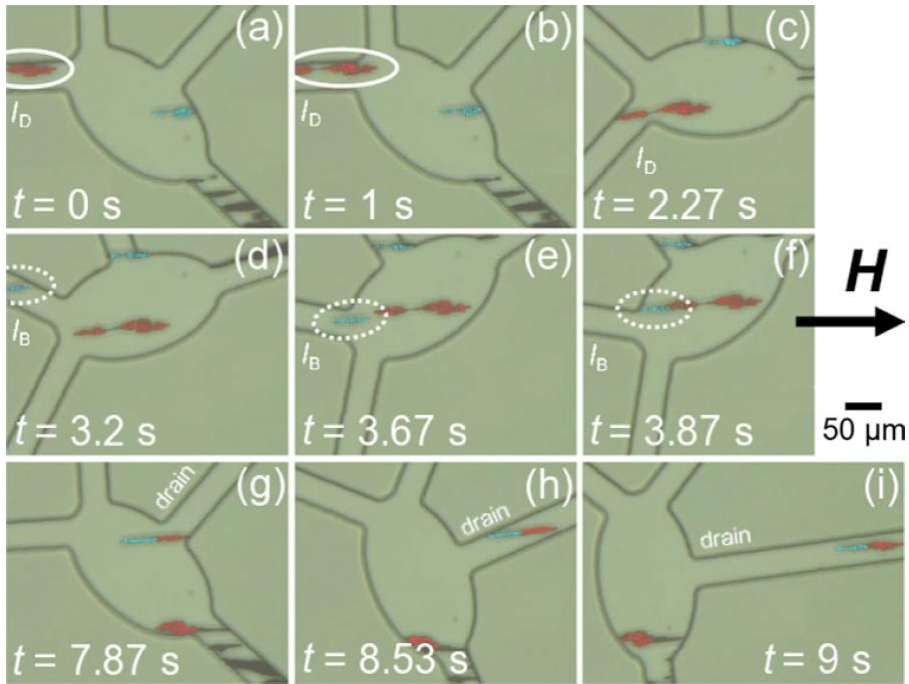
Fig. 5.3: Sequence of optical microscopy images which show a typical fill/drain process of the microfluidic device. Particle flow can be controlled by the orientation between external magnetic field and the fluid flow direction. (a-c) A bead chain which consists of Dynabeads® M-280 (red) enters the reaction site. (d-f) MyOne™ agglomerates may flow to the reaction chamber if the appropriate orientation of magnetic field and fluid flow direction is realized. (g-i) Bead chains merge at the reaction site and afterwards travel through the drain channel as confined objects. Residual fragments may remain at the reaction site.

chamber. For further applications, the geometry of the reaction site needs to be optimized to allow for a more efficient formation of superstructure and inhibition of breaking events during the rotation of the field. The reaction site may afterwards be washed through the waste channel and subsequent cycles of the fill/drain process can be performed. Additional effects can be identified, which result in an enhanced effectiveness of the device. The external magnetic field fixes the rotational degree of freedom of an agglomerate along the axis perpendicular to the sample plane. However, the rotational degree of freedom along the chain axis is not affected by the magnetic field. As shown in figure 5.4(a) this degree of freedom allows to enhance the stability of the chain agglomerates due to interaction with the carrier liquid. A chain within the reaction chamber which interacts with the channel wall may rotate along the chain axis to obtain a geometric configuration where the interaction with the fluid flow and, thus, shear stress along the chain is minimized. To ease the
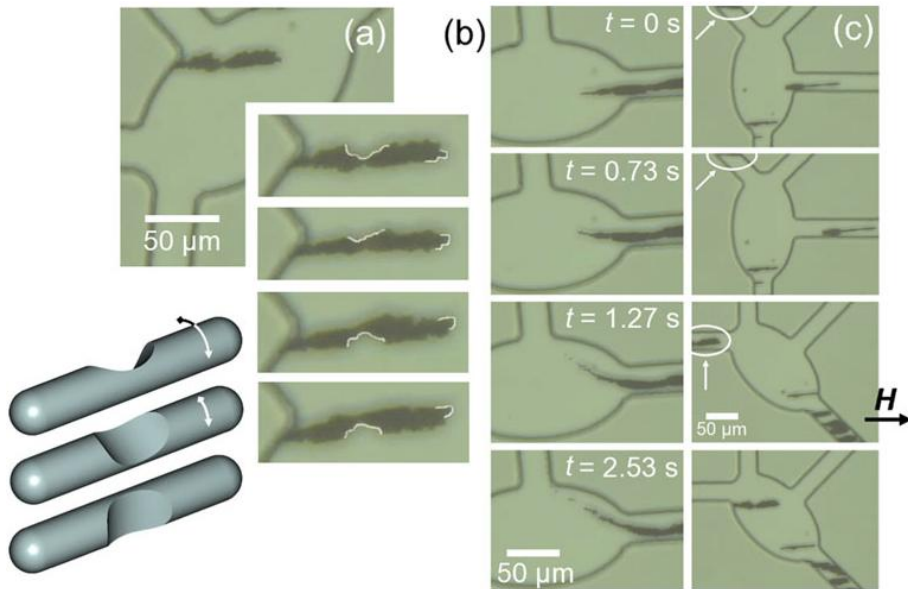
Fig. 5.4: Additional phenomena which entail a higher efficiency of the device. (a) Agglomerates blocked at positions within the reaction chamber may enhance their stability by rotation along the chain axis due to the interaction with the carrier liquid. (b) Disassembly of particle chains occurs on time scales of several seconds which can be necessary for specific applications. (c) Blocking events at the inlet channels depend on the angle between magnetic field and fluid flow direction.

tracking of the rotation along the long axis of the chain, the contour line of the agglomerate is highlighted. The movement can be interpreted as schematically presented in figure 5.4(a). If the external magnetic field is switched off, the superparamagnetic behavior of the employed beads enables a rapid disassembly as presented in figure 5.4(b). The particle agglomerates decay on time scales of several seconds. Therefore, a particle mixture prepared at the reaction site may be disassembled and afterwards act as a suspension of individual particles when washed out through the drain channel, if the actual application after the preparation at the reaction site demands isolated particles.

In addition blocking events as already explained above can be observed (figure 5.4(c)). The efficiency of blocking of chains in inlet channels depends as can be seen in figure 5.1(a) on the angle between the microfluidic channel axis and the magnetic field direction, but also on other parameters, such as the Mason number, geometric properties of the beads, the flow profile, and the surface properties of the beads and the channels. A more detailed analysis of these critical parameters is missing up to now, but will play a vital role in the further investigation of the proposed device. The critical values for the mentioned parameters will have to be determined for the

application of the reaction chamber since these values determine the applicability of the device.

In conclusion, dipolar coupling of superparamagnetic particles can be employed for the control of particle flow in a microfluidic system. The magnetic assembly of particle superstructures under the influence of a static magnetic field allows to inhibit the particle flow on demand on the basis of interaction between the magnetic agglomerations and channel walls at reservoir-channel junction. The operation of the proposed microfluidic device is demonstrated by employment of magnetic beads of different sizes, which allow for the optical tracking of individual beads and bead assemblies flowing from different reservoirs. Furthermore, the fill/drain procedure of the integrated reaction chamber is presented, which includes additional effects, such as flow-induced reorientation and on-demand disassembly leading to an enhanced stability of the device operation. Future works need to focus on the stability criteria of device operation with respect to experimental parameters, such as *Mn*, the flow profile of the carrier liquid and surface properties of beads and channels.

5.2 Enhanced fluid mixing and separation of magnetic bead agglomerates based on dipolar interaction in rotating magnetic fields

The applicability of magnetic agglomerates in stationary magnetic fields is presented in the previous section. In this chapter, we propose a microfluidic device which enables enhanced fluid mixing and colloidal separation based on the formation of one- and two-dimensional, rotating superstructures of superparamagnetic beads in a rotational magnetic field. Both functional tasks are based on the motion of magnetic bead agglomerates in a rotating magnetic field. The proposed structure utilizes free-flowing dynamically assembled components as active micromixers. The separation is based on the interaction between rotating magnetic bead agglomerates and the topological features of the microfluidic geometry. Based on a similar mechanism, the control of the particle flow was already demonstrated in the previous section. As described in chapter 4, the application of a rotating magnetic field favors the formation of highly ordered two-dimensional agglomerates which consist of large particle numbers. These large agglomerates are beneficial for the efficiency of the separation of the device as presented in the following. A schematic overview of the proposed device is shown in figure 5.5(a): Under the influence of an external, homogeneous rotating magnetic field the beads form chains that rotate with the field frequency. At the T-junction, enhanced mixing of fluids flowing from the inlet reservoirs is achieved based on the rotational motion of the magnetic agglomerates. The separation junction is represented by a barrier between two diverging channels.
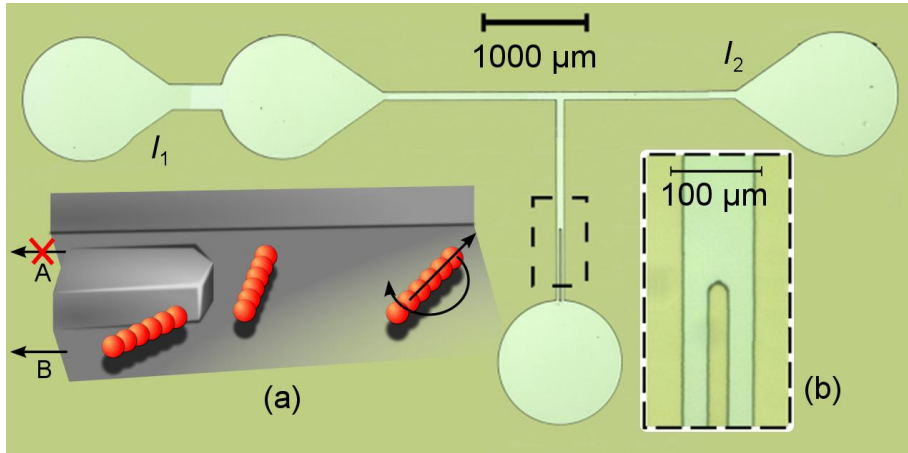
Fig. 5.5: Microscopy image of the SU 8-3025 casting mold. The inset (a) shows the operation principle of the microfluidic gate: Under the influence of a rotating magnetic field, the agglomerates are guided to either of the two diverging channels depending on the orientation of the rotation at the moment of contact with the barrier between the channels. Therefore, the particle flow is restricted to one of the two channels. (b) Magnification of the area where the guidance of beads at the separating barrier takes place.

The rotation of the chain leads to a transversal movement into one of the two channels, depending on the rotation direction. If no field is applied, individual particles are distributed statistically over both channels.

Experimentally, the proposed microfluidic device was realized by Bernhard Eickenberg in the framework of his Master's thesis (Eickenberg 2010). A microfluidic structure as shown in figure 5.5 was realized by soft-lithography techniques according to the procedure described in 3.1. Two inlet reservoirs I_1 and I_2 are connected by microfluidic channels of 77 µm width to a T-junction. Along this intersection area, the mixing capabilities of the device are demonstrated. The main channel which contains the separation junction is 79 µm in width and branches into two diverging channels of 28 µm width separated by a 23 µm wide barrier. Liquid flow through the device is generated by hydrostatic pressure. In the experiments, superparamagnetic Dynabeads MyOne^{TM} with a mean diameter of 1.05 µm and a carboxylic acid coating were chosen as magnetic particles.

A concentration of 120 µg/ml is achieved by dilution of the 10 mg/ml stock solution with deionized water and filled into the bead reservoir I_1 of the structure. The reservoir I_2 on the opposite side of the T-intersection is filled with a 65 mM flavin adenine dinucleotide (FAD) solution to allow for the optical evaluation of the interface layer between the two laminar flows. The rotating magnetic field necessary for chain formation and subsequent rotation of the superstructures is created by a
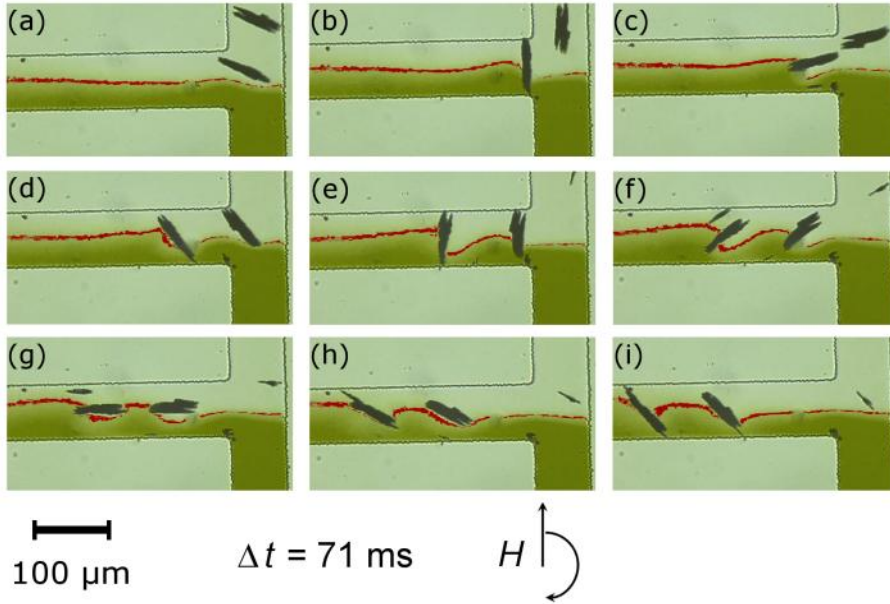
Fig. 5.6: Enhanced mixing effect induced by the rotation of magnetically assembled bead agglomerates. The interface between the liquids from the different inlet reservoirs I_1 (upper) and I_2 (lower) is highlighted (red) to ease the tracking.

magnetic stirrer with maximum in-plane field strength of 690 Oe as described in 3.3.2. This field strength leads to a degree of magnetic saturation of about 73% (Fonnum et al. 2005). The rotation frequency is set to 50 rpm throughout the whole experiment. At the chosen frequency, a stable rotation of the magnetic stirrer is obtained. Moreover, the stability of bead chains exposed to a rotating magnetic field decreases with increasing field frequency as was already demonstrated in chapter 4. Therefore, the chosen field frequency entails enhanced stability at high concentrations of bead chains. The amount of chains (transversal width of one or two beads) and clusters (transversal width of three or more beads) passing through either of the channels is counted separately. In case of chain or cluster breakage at the barrier, the superstructure was counted as flowing through both channels. Flow velocities are evaluated by tracking of superstructures in the channel.

The behavior of the fluid profile at the mixing junction under the influence of a rotating magnetic field is shown in figure 5.6. If no magnetic agglomerates pass the junction, thermal diffusion is the only driving force for the mixing of the liquids flowing from the inlets I_1 and I_2 (figure 5.6(a)). The assisting effect of bead agglomerates that pass the junction is presented in figure 5.6(b-i): due to a finite viscosity of the fluids, the rotation of a bead chain induces a laminar flow nearby its position. For a clockwise rotation, such fluid flow entails a convective flux from the
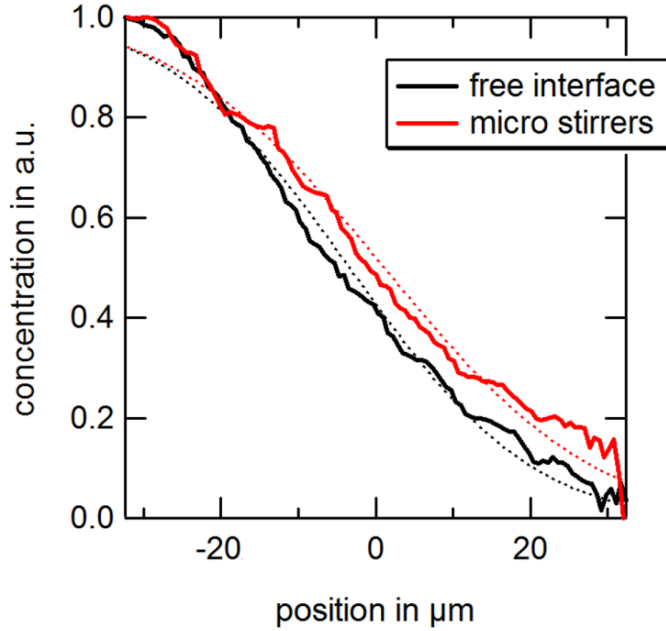
46

Fig. 5.7: Clockwise rotating magnetic bead chains increase the mixing of FAD solution and water. Resulting concentration profile in comparison to a thermal reference.

FAD-phase into the deionized water phase in the traveling direction of the superstructure and vice versa behind it. The interface between the two liquids from the different inlet reservoirs I_1 and I_2 is highlighted to ease the tracking. One and two-dimensional bead agglomerates act as free-flowing magnetic micro stirrers. In order to quantitatively analyze the influence of these free-flowing magnetic microstirrers, the intensity profiles of the FAD solution 310 µm downstream from the T-intersection are evaluated. The resulting data are compared to the analytic solution of free diffusion across an interface (2.22) to evaluate the effective diffusion constant D_{eff}. As shown in figure 5.7, the diffusion constant of sole thermal diffusion results in a value of $D_0 = 3.04 \times 10^{-10}$ m²/s which is in very good agreement with the finding of Radoszkowicz et al. (2011) who reported $D_0 = 3 \times 10^{-10}$ m²/s for the diffusion constant of FAD in water. Under the influence of rotating bead chains, an increase to $D_{eff} = 4.02 \times 10^{-10}$ m²/s is found corresponding to a diffusivity increase by 32%. The dotted lines in figure 5.7 show the resulting concentration profiles according to (2.22) which are employed for the calculation of the respective effective diffusion constants. Along the separation junction, bead assemblies are guided due to their interaction with the channel walls as schematically shown in figure 5.5(a). Agglomerates are guided to channel A or B depending on whether the rotation of the external magnetic field is counter-clockwise or clockwise, respectively.
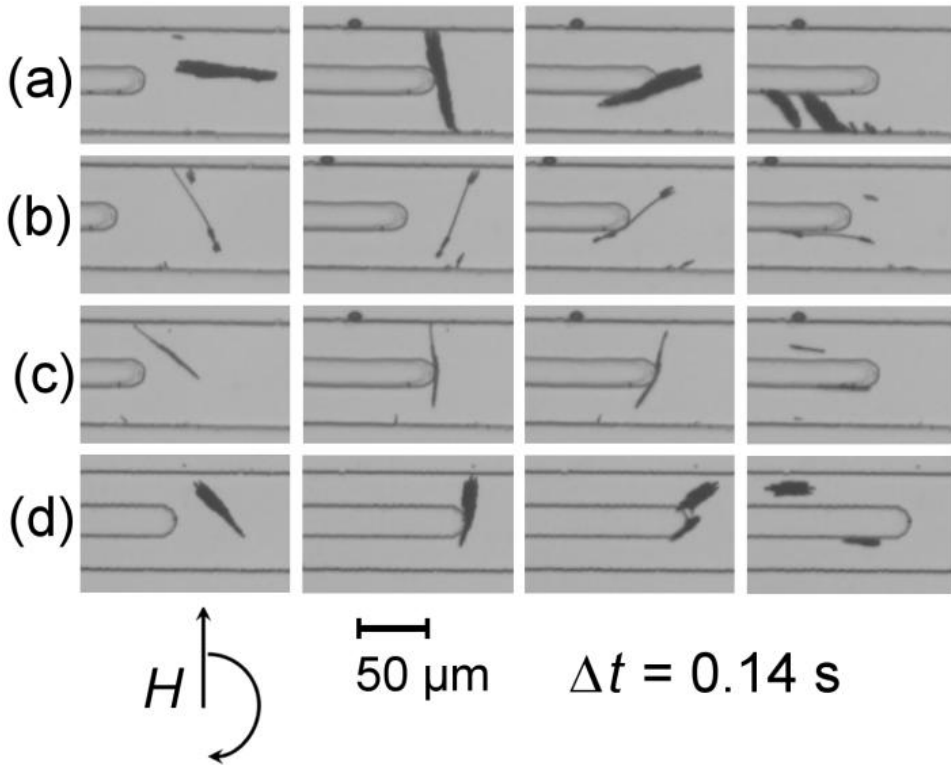
Fig. 5.8 (a) Movement of a rotating cluster structure composed of aggregated MyOne^TM beads that is guided to the lower channel through the influence of the (clockwise) rotating magnetic field at a flow velocity of about 250 μm/s. (b) Successful guidance of a chain superstructure into channel B at a flow velocity of 240 μm/s. (c) At a flow velocity above 160 μm/s a chain superstructure breaks apart at the barrier due to high shear stresses that occur when the agglomerate interacts with the channel wall. (d) A cluster structure breaks apart at a flow velocity of about 200 μm/s.

Figure 5.8 presents a series of optical microscopy images which show the successful guidance of chain superstructures (figure 5.8(b)) and clusters (figure 5.8(a)) as well as the breakage of superstructures at the barrier (figure 5.8(c,d)). Breakage events occur due to shear induced stresses if agglomerates interact with the channel wall by steric repulsion. The flow velocities for the cases mentioned above are in the range between 160 μm/s and 250 μm/s. In this velocity regime, the breakage of superstructures reduces separation efficiency (figure 5.10). Additionally, the presence of small fragments with a lateral dimension smaller than the channel width entails a lowered separation efficiency. These fragments do not interact with the barrier during rotation and, therefore, no guidance is performed. In contrast to the breakage events, the formation of these small fragments can be observed for all flow velocities that

48

were investigated, whereas the breakage of superstructures was not observed in the regime of flow velocities below 63 µm/s. Due to the small size of the fragments, the effect on the separation efficiency is, nevertheless, insignificant, as can be seen from the high separation yield throughout the experiments. The concentration of these small fragments may be tailored by the choice of suitable magnetic bead concentrations since higher bead concentrations entail the formation of larger two-dimensional agglomerates (chapter 6).

Even for large two-dimensional agglomerates, the separation at the barrier is achieved. As depicted in figure 5.9, large agglomerates are sorted and break apart afterwards. In the experiments, no blocking of the diverging channel was observed by the employment of the above mentioned bead concentration of 120 µg/ml.

The efficiency of the device is evaluated for the clockwise rotation direction. Figure 5.10(a) shows the fraction x of superstructures and beads that are successfully guided to channel B as a function of the flow velocity. At mean flow velocities of 42 µm/s and 63 µm/s, a high fraction of well above 90% of the superstructures is obtained. Particles that pass the junction area via channel A can be attributed to small fragments which do not interact with the device walls as mentioned above. At a higher mean flow velocity of120 µm/s, the yield slightly decreases to 89%.

At this point, the probability of chain breaking due to higher shear stresses is
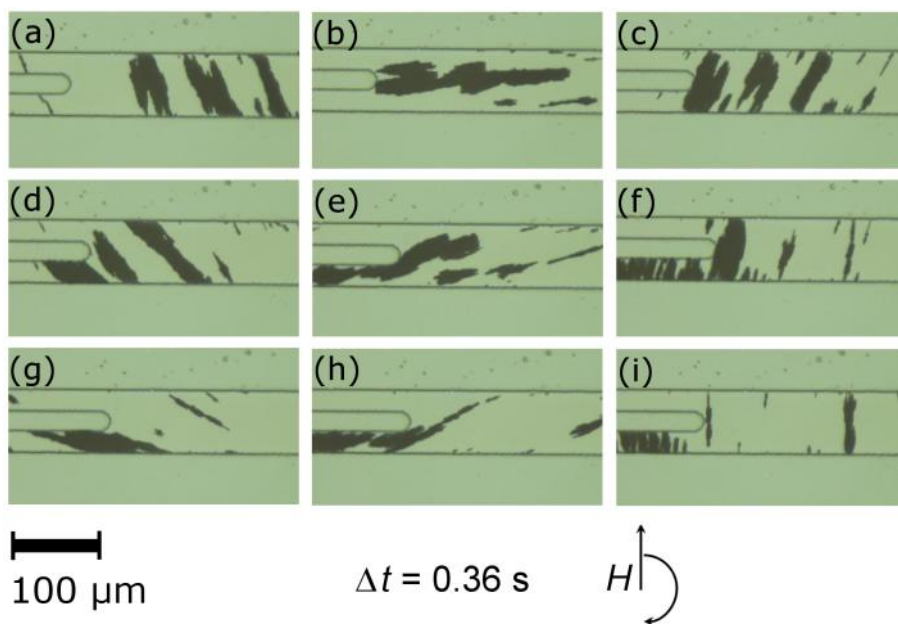

Fig. 5.9: Separation of large two-dimensional agglomerates at the separation junction under rotation of the external field.

increased, which decreases the amount of sorted chains to 71%, while the larger part of the clusters (84%) maintains stability against steric repulsion and is, consequently, guided to channel B. At significantly higher flow velocities (274 µm/s), breakage of clusters reduces the fraction of clusters in channel B down to 61%. In addition, high flow rates allow for clusters to bypass the junction area without completion of a 180° rotation; superstructures reach channel A without contact with the barrier. Consequently, in order to obtain higher throughput rates, higher field frequencies are required to provide sufficient cluster-wall interaction. However, the possibility to further increase the rotation frequency is limited, because the stability of the agglomerates needs to be maintained. Still, a significant fraction of 63% of the total bead number is successfully manipulated by the developed gate structure.

For further analysis of the device, we define the separation efficiency ε by

$$\varepsilon = 2x - 1 . \tag{5.1}$$

The efficiency defined above takes into account that without a magnetic field applied the expected fraction of beads in channel B would be 50% and, therefore, the separation efficiency would vanish. The dependence of ε on the flow velocity is presented in Fig. 5.10(b). If the flow velocity increases, the efficiency decreases due to higher shear stresses as mentioned above. For flow velocities up to 120 µm/s, efficiencies between 0.92 and 0.77 are obtained. A further increase of the flow velocity leads to an additional decrease in the separation efficiency. However, due to the higher flow velocity larger, volumes pass the separation junction so that larger amounts of beads are transported. To take this effect into account, we introduce the mass separation rate ξ by

$$\xi = \Gamma \, c_{\text{bead}} \, \varepsilon \tag{5.2}$$

with c_{bead} the bead concentration in the solution and $\Gamma = |u| \, a$ the volume flow rate depending on the flow velocity $|u|$ and the geometry parameter a. The bead concentration c_{bead} and the geometry parameter a depend on the experimental details, which we summarize by the experimental parameter

$$\alpha = c_{\text{bead}} \, a . \tag{5.3}$$

Since the geometry parameter a depends on the details of the flow profile, which itself strongly depends on the exact geometry of the channels, the comparison of different channel geometries is difficult, if only the mass separation rate is discussed. Therefore, we divide (5.2) by (5.3) and obtain

$$\frac{\xi}{\alpha} = |u| \cdot \varepsilon \ . \tag{5.4}$$

Figure 5.10(c) shows the behavior of the quantity ξ/α under variation of the flow velocity. Because ξ/α takes all flow velocity dependent effects into account, it is a proper measure for the evaluation of the optimal working regime of the proposed device if both throughput and separation efficiency are of similar importance for the actual application. If the application focuses either on a high separation efficiency or on high throughput, additional weighting factors need to be introduced to (5.2), which will not be taken into account in the following. As depicted in Figure 5.10(c), we obtain an increasing device efficiency for flow velocities from 42 µm/s to 120 µm/s. The employment of a flow velocity of 274 µm/s entails lower efficiencies. Thus, we may conclude that the maximum mass separation ratio and, consequently, the most efficient working regime of the proposed device lies between 63 µm/s and 274 µm/s for the chosen rotating magnetic field operation frequency of 50 rpm.

The developed microfluidic device allows to enhance fluid mixing and separation of magnetic bead agglomerates simultaneously. If free-flowing magnetic microstirrers are present, the mixing of two fluid streams is enhanced due to the interaction of the magnetic entities with the carrier liquid. Quantitatively, the mixing enhancement can be determined based on the simple analytical model of diffusion across an interface and allows to estimate the increase of the diffusivity of FAD to 32% if magnetic microstirrers are employed.
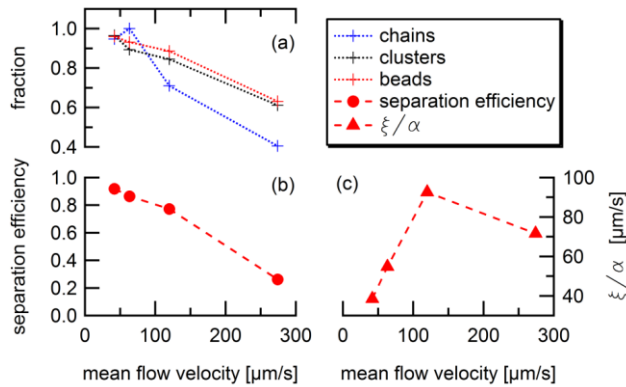

Fig. 5.10: Evaluation of the separation performance. (a) The fraction of clusters, chains and beads in superstructures decreases with increasing mean flow velocity of the carrier liquid. (b) For the separation efficiency, a decrease with the mean flow velocity is obtained. (c) The quantity ξ/α allows to evaluate the optimal working regime of the structure, which reveals that the maximum of the mass separation rate is obtained in the velocity range between 120 µm/s and 274 µm/s.

The proposed separation principle allows to achieve high separation efficiencies at lower flow velocities. The yield decreases with increasing flow velocity mainly due to the higher probability of chain and cluster breaking induced by shear stresses. However, if the increasing volume flow rate is taken into account, an optimal working regime of the device between 63 µm/s and 274 µm/s at a rotation frequency of 50 rpm may be identified. Current and future works, which are partly already conducted by Bernhard Eickenberg, need to focus on the dependence of the device efficiency on the magnetic field strength and the rotation frequency of the magnetic field. This investigation will, consequently, also allow to the estimate the dependence of the efficiency of the microfluidic device on the Mason number.

6 Surface patterning based on magnetically induced self-assembly of magnetic particles

In the previous chapters, the fundamental behavior and dynamics of dipolar coupled magnetic superstructures and their applicability in the framework of microfluidic application have been presented. In addition to the applicability in microfluidic applications, the highly ordered structures may also be employed in surface patterning. For that purpose various aspects, such as transfer of the highly ordered structure from the liquid phase to the evaporated sample, size of resulting agglomerates, defect structure and their dependence on the experimental parameters need to be addressed. The findings on surface patterning in rotational magnetic fields are summarized in this chapter and were published in (Weddeman et al. 2010 a) and (Wittbracht et al. 2012 b).
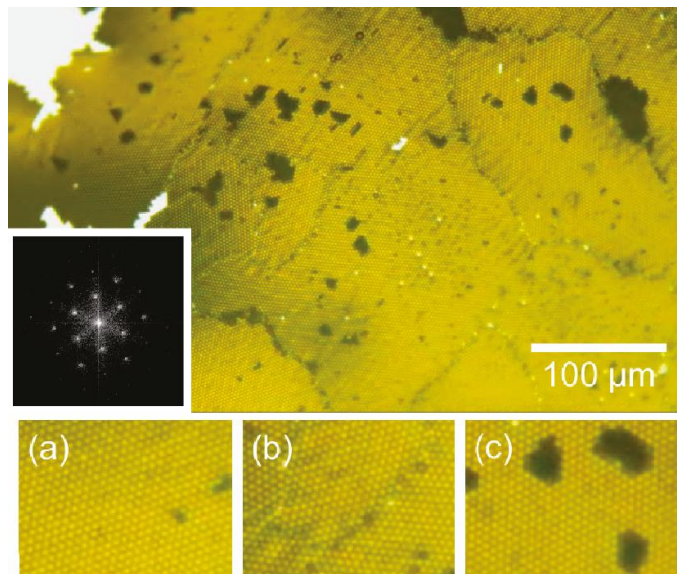

Fig. 6.1: Monolayer of magnetic beads which results from the magnetic field induced assembly process. The grayscale inset shows the FFT of the particle grid positions which reveals the strongly pronounced hexagonal symmetry. (a) Areas without defects in the monolayer can be distinguished from (b) zero- and one-dimensional defect structures. (c) Particles within the second layer of agglomerates can be identified since they appear as dark spots.

Experimentally, the assembly method is investigated by spotting of suspension of Dynabeads® M-270 SA on a silicon wafer which itself is situated on the centre a magnetic stirrer hotplate. The employed magnetic stirrer setup allows for the generation of a magnetic field strength of up to 330 Oe at the sample position. Three different dilutions of the stock solution of the beads are prepared at 0.2, 1.0, and 5.0 mg/ml and rotation frequencies of 400 rpm 800 rpm and 1200 rpm are investigated. Our preliminary experiments revealed that during evaporation of the liquid salt crystallization strongly hinders the ordering process. Therefore, the PBS buffer in the stock solution is exchanged with DI-water by subsequent centrifugation and resuspension.

Figure 6.1 shows a particle agglomerate which results from the magnetic field induced assembly in the liquid phase before evaporation of the carrier liquid. Large areas of highly ordered monolayers can be identified as supported by the inset in figure 6.1 (upper) which depicts the corresponding FFT of a highly ordered region. Strong hexagonal ordering of the superstructures can be observed. The insets (a-c) in figure 6.1 show several details concerning the ordering in the superstructures. Figure 6.1(a) shows a region of the agglomerate with negligible defects, whereas figure 6.1(b) represents an example of an agglomerate region with zero- and one-dimensional defects. In particular, the one-dimensional defects introduce a grain-like structure in the agglomerates, which is comparable to the case of grain boundaries in nanostructured material (Ovid'ko 2004). Dark spots in figure 6.1(c) represent particles which assembly in the second layer of the agglomerate. Approximately 5% of all particles in the agglomerates grow in the second layer. Therefore, it can already be concluded that the proposed method is suitable for the generation of highly ordered two-dimensional particle layers. In liquid phase, no breaking of clusters is observed after the assembly. However, in our experiments, the liquid evaporation results in high shear stresses as the contact line between substrate and liquid moves along the surface. Therefore, closed particle layers break under the induced shear stresses, which results in smaller agglomerates. In order to allow to form larger monolayers with reduced amount of defects, different liquids with a lower surface energy need to be tested in future experiments. In contrast to the induction of lattice impurities based on liquid evaporation another mechanism which leads to defect structures is based on the reordering dynamics during agglomerate formation in the liquid phase. In figure 6.2(a) the absorption of a particle chain to a previously formed cluster due to dipolar particle coupling (Hayes et al. 2001) is presented. As can be seen in the image sequence the approaching particle chain breaks prior to absorption and reordering processes along the rim of the cluster structure can be observed. Due to the reordering the cluster remains without defects, even after the particle chain was absorbed. In contrast to the process of chain absorption, the merging of clusters results in the creation of additional defect structures. In figure 6.2(b) a multi-fragment agglomerate is presented which results from the merging of previously
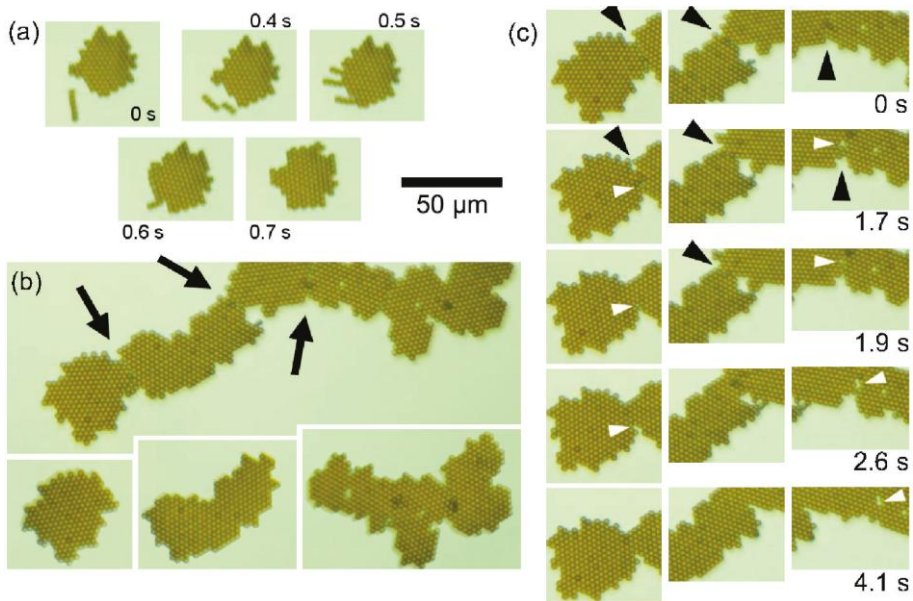
Fig. 6.2: Sequences of optical microscopy images, which show the reordering processes during the growth of cluster structures. (a) The absorption of a magnetic particle chains to a previously formed cluster allows for the growth of the cluster structure without introducing additional defects. (b) Merging process of clusters, the insets show individual fragments which assembly to a larger cluster object. The arrows indicate regions with ordering defects which result from the merging of the fragments. (c) The time evolution of monolayer structures under the influence of the external magnetic field reveals that reordering processes occur along the marked regions. While one-dimensional defects (black arrows) are reduced by the external perturbation, isolated vacancies (white arrows) are created during the process.

formed clusters. Insets show the fragments before the formation of the larger clusters. The arrows in figure 6.2(b) indicate the contact lines between the fragments which show a reduced symmetry. Under the influence of subsequent rotation of the external magnetic field, geometric and magnetic reordering leads to increased symmetry along the contact lines (figure 6.2(c), black arrows) until a stable configuration is achieved. This process of reordering may lead to isolated vacancies as can be seen in figure 6.2(c) (white arrows). The quantitative analysis of cluster growth and properties of the resulting clusters is based on the iterative replenishment of particle concentration after the agglomeration of superstructures and evaporation of the liquid. The data obtained from optical microscopy of the agglomerates after evaporation of the carrier liquid allows for the conclusion that the rotation frequency of the applied magnetic field does not influence the size of clusters within the frequency range of investigation. In contrast, the particle concentration strongly influences the size of the agglomerates as shown for the concentrations of 0.2 mg/ml
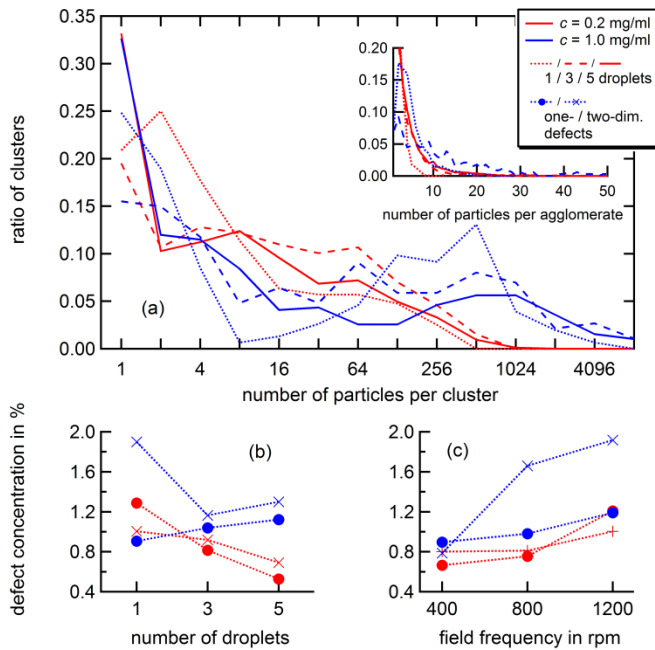
Fig. 6.3: (a) Cluster growth in dependence for 1, 3 and 5 iterative replenishments of droplets at particle concentrations of 0.2 mg/ml and 1.0 mg/ml. The inset shows the agglomerations obtained from the reference sample without magnetic field. Dependence of the defect concentrations in the ordered agglomerates resulting from magnetic field induces assembly. (c) The influence of the field frequency of the rotating magnetic field and (b) iterative replenishments of particle concentration are summarized.

and 1.0 mg/ml in figure 6.3(a). In the case of the reference sample, where the particle solution is spotted onto the substrate and liquid evaporation occurs without the influence of a magnetic field, the agglomerate size distribution depicted in the inset of figure 6.3(a) is obtained. The particles are randomly dispersed along the substrate. Ordering cannot be obtained from FFT images of the particle grid positions. If the spotting and liquid evaporation is performed under the influence of an external rotating magnetic field, magnetic field induced assembly is entailed. Evaluation of the respective microscopy images leads to the agglomerate size distribution presented in figure 6.3(a). The influence of the magnetic field manifests itself under comparison of figure 6.3(a) with the inset. The comparison of, e.g. the samples prepared with 5 droplets of the $c = 0.2$ mg/ml suspension shows that without the field influence the maximum agglomerate size obtained from the microscopy is 16 particles, whereas due to the rotational magnetic field clusters which consist of up to 512 particles can be found.

Iterative replenishment of particle concentration to the samples entails a shift of the cluster sizes to higher particle numbers. Therefore, it can already be concluded

that the provision of additional particle concentration does not necessarily result in additional cluster formation, but may lead to the growth of already existing superstructures. A similar phenomenon occurs in the context of the Ostwald ripening in nanoparticle fabrication (Ostwald 1896), where also the formation of few large particles is favored over the assembly of many small particles.

In figure 6.3(b-c) the defect concentration of the resulting assemblies is presented. In case of low particle concentration within the suspension, the replenishment of particle concentration onto the substrate allows for a decrease in the defect concentration (figure 6.3(b),red). The trend holds for zero- and one-dimensional defect structures. However, if the particle concentration within the suspension increases (figure 6.3(b),blue), the provision of additional particle concentration results in an increased defect concentration. The underlying mechanism can be understood together with the observation of the cluster merging dynamics presented in figure 6.2(c): Since the increase in particle concentration results in less accessible free volume, reordering processes are inhibited. Therefore, above a certain critical particle concentration, the provision of additional particles entails an increased defect concentration. If the rotation frequency of the magnetic field increases, an increasing
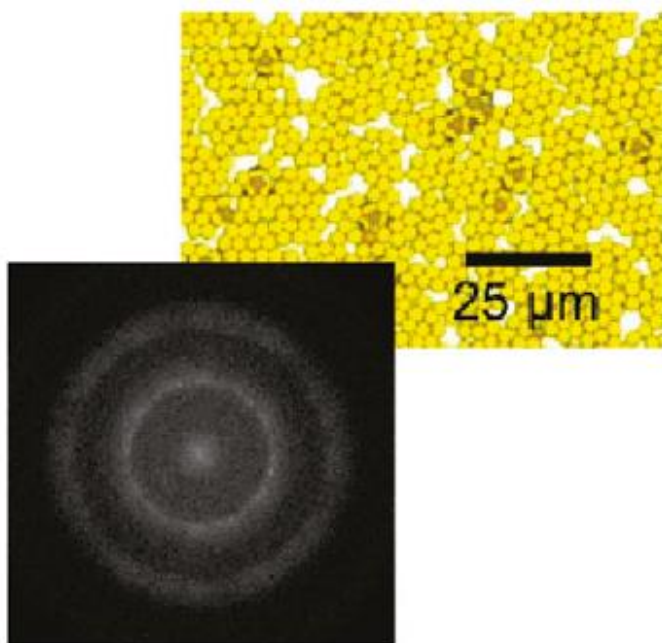

Fig. 6.4: Microscopy image and corresponding FFT of the particle grid positions for the reference samples which are prepared with $c = 5.0$ mg/ml without the employment of a magnetic field. No spatial ordering of the particles can be found.

defect concentration is obtained as displayed in figure 6.3(c). The trend of the defect concentration in figure 6.3(c) can be explained by differing reordering time scales. The transition to structures of higher symmetry as displayed in figure 6.2(c) and, therefore, lowered defect concentration is limited since the geometric reordering cannot follow the transient magnetodynamics.

The growth of layers of magnetic beads is studied based on the employment of the highly concentrated particle suspension ($c = 5.0$ mg/ml). One example of a resulting layer is presented in figure 6.1 which was already discussed above. As already mentioned, one dimensional defects entail a grain structures within the sheets of high local symmetry.

The microscopy images and corresponding FFT images presented in figure 6.4 suggest that such highly symmetric regions cannot be found in the reference samples prepared without the application of the magnetic field. Therefore, the analysis will be restricted to the samples prepared without a rotating magnetic field. Figure 6.5(a) shows the grain size distribution, which is obtained from optical microscopy of the evaporated samples. For these high particle concentration samples, the additional provision of particles results in a decreased grain sizes as can be seen
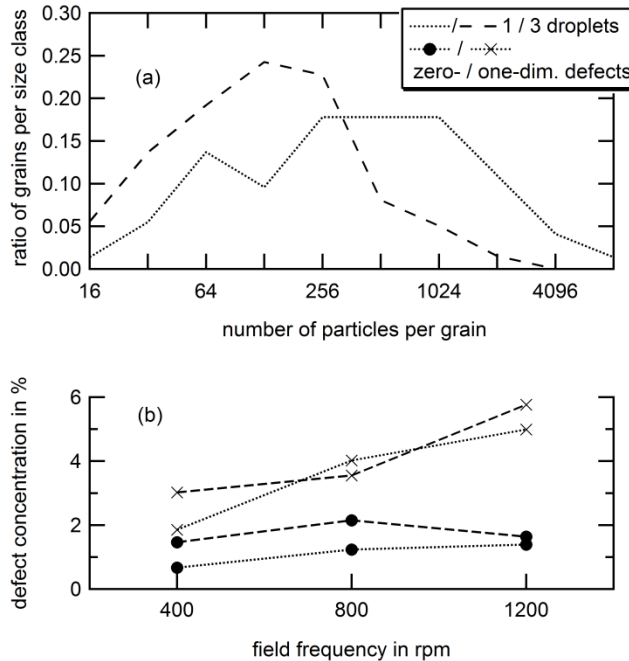

Fig. 6.5: (a) Grain size distribution of the agglomerates prepared with magnetic field at a particle concentration of $c = 5.0$ mg/ml. (b) Dependence of the defect concentration of agglomerate layers prepared with particle suspensions at a concentration of $c = 5.0$ mg/ml on the rotation frequency of the magnetic field.

by comparison of the dotted (1 droplet) and dashed lines (3 droplets) in figure 6.5(a). The behavior can be understood equivalent to the argumentation in context with the cluster growth and the increasing defect concentration for high particle concentration suspensions (figure 6.3 (b)). The lowered free volume for reordering processes inhibits the reorganization and, therefore, a lowered symmetry in the assemblies is entailed. Consequently, since the grain size is reduced for higher number of particles on the substrates, the defect concentration increases as presented in figure 6.5(b). Again, a lower rotation frequency of the external magnetic field favors the formation of agglomerates with lower defect concentration.

If a suspension at a concentration of $c = 5.0$ mg/ml is used and three droplet are spotted under the influence of the magnetic field, the average grain size of the resulting assemblies is 463 particles. This particle number corresponds to an area of ~2850 μm^2.

The spotting and liquid evaporation procedure for such arrays takes about 15 minutes. A similarly large area of highly ordered particle agglomerates could also be prepared by Riley and Lidell (2010). The author show highly ordered assemblies with areas of about 2900 μm^2. However, since their approach for the fabrication of the particle patterns is based on sedimentation, the production of large assemblies is time consuming. In contrast, our approach is not only fast, but also easy to control since the formation can be started by the initiation of the magnetic stirrer rotation. Furthermore, the rotating magnetic field might also be realized with a coil setup
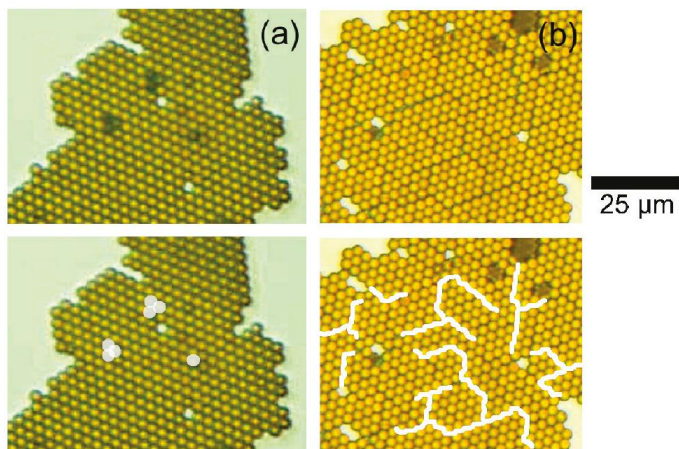
Fig. 6.6: Optical microscopy images of clusters assembled under the influence of a rotational magnetic field. (a) If second layer growth of the highly ordered structures can be found, the multilayer sequence is found to be AAA-sequence which may be attributed to magnetic coupling. (b) After evaporation of the carrier liquid, the shear stresses which act on cluster, while the contact line at the liquid solid gas interface moves, lead to cracks in the cluster which usually occur along straight lines.

which allows to assemble and disassemble on demand similar to the approach presented in 5.1.

After the detailed analysis of the monolayer growth and defect concentrations, additional effects will be presented and discussed. As already mentioned in context with figure 6.1(c), the second layer growth is small. Nevertheless from the dynamic video microscopy of agglomerates in the liquid phase an interesting feature of the second layer growth can be observed. As previously explained, the clusters show hexagonal symmetry. However, if second layer growth occurs, this geometrical ordering is not continued. From geometric effects a stacking of ABCABC… or ABAB… would be expected for the out-of-plane growth direction. As presented in figure 6.6(a) this stacking is not present, but AAA… stacking can be found. Since steric effects would be assumed to lead to a stacking of ABCABC…. or ABABA…, the AAA… stacking may result from the dominant magnetic coupling between the beads as was also reported by Albon et al. (2009). While the carrier liquid evaporated and the contact line between the liquid-air-interface moves along the substrate, strong capillary-induced shear stresses arise. These shear stresses overcome the magnetic coupling between beads and lead to breakage of the clusters immediately before the solvent evaporates completely. The resulting structures show characteristic straight lines along which the breaking of particle film occurs. In order to understand this behavior Alexander Weddemann simulated the magnetic equilibrium state of a dipolar coupled 13×13 particle grid. A numerical model is applied, where each magnetic bead is described by a particle of homogeneous magnetization $M_S = 300$ kA/m. The detailed method of simulation can be found in (Weddemann 2010 c). The resulting magnetic equilibrium state is presented in figure 6.7.
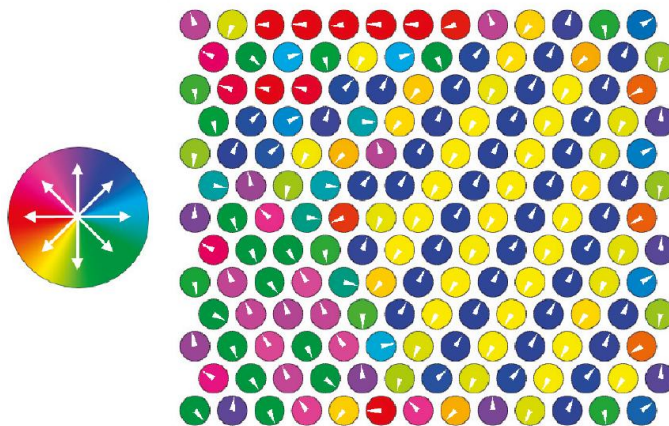

Fig. 6.7: Magnetic equilibrium state of a 13×13 particle grid assuming homogeneously magnetized and dipolar coupled particle volumes. Domain-like regions of antiparallel magnetic orientation can be found.

The color code shows the in-plane component direction of the magnetic moment of each individual particle. According to the simulation results, the out of plane components may be omitted. The magnetic moments form regions comparable to magnetic domains in the solid state. By formation of such domains or domain-like regions, the stray field energy is minimized. The magnetic orientation of domains is often antiparallel, which minimizes the stray field between the domains. Therefore, regions of stronger and weaker coupling may be found within clusters. If the liquid evaporates the regions of lower coupling may lead to the characteristic breakage along straight lines as presented in figure 6.6(b).

In summary, the assembly of superparamagnetic beads in a rotational magnetic field may be used for the generation of highly ordered arrays of particles. Based on the magnetic interaction between particles and resulting agglomerations, the particle growth occurs on time scales of several tens of seconds to few minutes. In dependence on the rotation frequency of the applied magnetic field, hexagonally ordered two-dimensional structures with grain sizes up to 2900 μm^2 can be produced. The concentration of zero- and one-dimensional defects can be controlled via the rotation frequency of the external field and the particle concentration on the substrate. Iterative concentration replenishment during the self-assembly procedure allows to initiate the growth of existing particle clusters similar to the Ostwald ripening mechanism in nanoparticle fabrication. Only a small amount of second layer growth is observed. However, this growth mechanism seems to be governed by magnetic forces, since the stacking sequence is AAA… and not ABAB… or ABCABC… as expected from geometrical aspects. Under evaporation of the carrier liquid, assemblies may break along straight lines, which can also be explained by the magnetic substructure within the assemblies. As a simple numerical model suggest, the breaking event occur along lines of reduced coupling and, consequently, decreased forces act along these regions, which results in breakage under shear stresses.

Currently the transfer of the assembly mechanism from micron-sized particles to nanoscale particles is under discussion. The results of a first approach conducted in our workgroup can be found in (Regtmeier et al. 2012). Future works in context with the proposed mechanism for particle assembly will need to investigate the influence of the surface tension of the carrier liquid in more detail in order to reduce shear stress induced sheet breakage during liquid evaporation. Furthermore, calculation of the coupling forces inside the sheets based on the already conducted and presented simulations (Weddemann et al. 2010 b) would be helpful to understand the stability of the agglomerates in more detail.

7   Summary

In summary, it was shown that the direct coupling of magnetic particles may be employed in microfluidic applications and can lead to a beneficial behavior of the proposed devices. Starting from a fundamental study on the formation dynamics of dipolar coupled superstructures, objects are classified according to their dimensionality and respective formation time scales are obtained. Two-dimensional cluster and one-dimensional chain objects may be differentiated. The main process responsible for the growth of clusters is the collapse of chain structures induced by viscous drag forces which result from the rotation of chains under rotation of the external homogeneous magnetic field. According to our experimental results, the chain dissociation rate was determined to be linearly connected with the rotation frequency of the external magnetic field and therefore also linearly dependent on the Mason number. The result is in good agreement with the findings of Petousis et al. (2007) who also reported a linear dependence of the chain stability on the Mason number in a similar regime of Mason numbers.

The magnetic field induced assembly of magnetic superstructures may be used for the application of particle flow control in microfluidic devices as presented in chapter 5.1 if a stationary magnetic field is employed. Depending on the relative orientation of microfluidic channels and the previously formed magnetic agglomerates in the carrier liquid stream, the flow of particles may be inhibited. Therefore, the particle flow and the flux of the carrier liquid have to be uncoupled by interaction of agglomerates with the channel walls. The proposed microfluidic device combines an elliptical reaction chamber with two inlet and two outlet channels and allows for the selective transport of particle species towards the reaction site. In the reaction chamber merging of agglomerates and subsequent collection of the product in a drain channel can be performed.

Based on the findings on the formation dynamics of magnetic superstructures in rotating magnetic fields, a microfluidic device which allows for fluid mixing and subsequent colloidal separation from the suspension was developed. The separation junction of the device consists of a branching channel, where the separation mechanism is based on the interaction of particle agglomerates with the barrier at the branching junction. In dependence on the rotation direction, the flow into one of the daughter channels may be inhibited. The separation efficiency of the device strongly depends on the flow velocity of the carrier liquid, because the hydrodynamic shear stresses on particle agglomerates, which interact with the barrier, increase with the

62

flow velocity. If the volume flow rate is taken into account, the optimal working regime of the microfluidic structure can be determined. We find for our experimental parameters of the rotating magnetic field, that the optimal regime of flow velocities for device operation at high mass separation efficiencies lies in the range between 63 μm/s and 274 μm/s. In future works, the dependence of the separation efficiency on the magnetic field strength and the rotation frequency of the magnetic field will be investigated. In particular, this will allow for the characterization of the proposed microfluidic device in dependence on the Mason number.

In addition to the guidance of particle agglomerates at the separation junction, the rotation of the agglomerates can be used for enhanced mixing application by introduction of a T-junction. Without the magnetic microstirrers, two parallel liquid streams are mixing by thermal diffusion only. Under the influence of rotation of the micro stirrers a convective flux between the liquid streams is entailed due to the interaction of the particle agglomerates with the carrier liquid. The mixing properties are evaluated in a model system with an aqueous magnetic bead solution and an aqueous FAD solution. Mixing efficiencies are obtained from intensity plots resulting from evaluation of optical microscopy data. The results are compared with the analytical solution for diffusion across an interface. This method allows for the determination of the FAD diffusivity in water and the enhancement of the diffusivity. If microstirrers are employed, an increase of about 32% of the FAD diffusivity is observed.

Besides microfluidic applications also surface patterning can be achieved by the employment of a rotating magnetic field. Highly ordered two-dimensional sheets of particles with sizes up to 2900 $μm^2$ can be prepared based on the magnetic field induced particle assembly. The defect structure of the resulting assemblies can be tailored by the rotation frequency of the employed particle concentration. Assemblies prepared in the carrier liquid break under liquid evaporation induced shear stresses along straight lines, which can be attributed to the magnetic interaction inside the sheets according to numerical simulations. Due to coupling of neighboring particles, domain-like regions inside the assemblies are formed. The breaking events occur along the edges of these domain-like regions.

References

Albon C, Weddemann A, Auge A, Meissner D, Jutzi P, Rott K, Hüten A (2009) Tunneling magnetoresistance sensors for high resolutive particle detection. Appl. Phys. Lett. 95(2): 023101

Auge A, Weddemann A, Wittbracht F, Hütten A (2009) Magnetic ratchet for biotechnological applications. Appl. Phys. Lett. 94(18):183507

Batchelor GK (2000) An introduction to fluid dynamics. Cambridge University Press, Cambridge

Bossis G, Lacis S, Meunier A, Volkova O (2002) Magnetorheological fluids. J. Magn. Magn. Mat. 252:224-228

Brigadnov IA, Dorfmann A (2005) Mathematical modeling of magnetorheological fluids. Continuum Mech. Thermodyn. 17:29-42

Bruus H (2008) Theoretical microfluidics. Oxford University Press, Oxford

Brzeska M, Panhorst M, Kamp PB, Schotter J, Reiss G, Pühler A, Becker A, Brückl H (2004) Detection and manipulation of biomolecules by magnetic carriers. J. Biotechnol. 112:25-33

Deng T, Whitesides GM, Radhakrishnan M, Zabow G, Prentiss M (2001) Manipulation of magnetic microbeads in suspension using micromagnetic systems fabricated with soft lithography. Appl. Phys. Lett. 78(12):1775–1777

Derks RJS, Frijns AJH, Prins MWJ, Dietzel A (2010) Multibody interactions of actuated magnetic particles used as fluid drivers in microchannels. Microfluid. Nanofluid. 9:357–364

Eickenberg B (2010) Verhalten superparamagnetischer Beads in rotierenden Magnetfeldern und ihre Verwendung zur mikrofluidischen Flusskontrolle. Master thesis, Bielefeld University

Einstein A (1906) The theory of Brownian Motion. Annalen der Physik 19(2):371-381

Ennen I (2008) Magnetische Nanopartikel als Bausteine für granulare Systeme: Mikrostruktur, Magnetismus und Transporteigenschaften. PhD thesis, Bielefeld University

Fonnum G, Johansson C, Molteberg A, Mørup S, Aksnes E (2005) Characterisation of Dynabeads® by magnetization measurements and Mössbauer spectroscopy. J. Magn. Magn. Mat. 293:41-47

Friend J and Yeo L (2010) Fabrication of microfluidic devices using polydimethylsiloxane. Biomicrofluidcs 4:026502

Furst EM, Gast AP (1999) Micromechanics of dipolar chains using optical tweezers. Phys. Rev. Lett. 82:4130-4133

Gast AP, Zukoski CF (1989) Electrorheological fluids as colloidal suspensions. Adv. Colloid. Interface Sci. 30:153–202

Gijs MAM (2004) Magnetic bead handling on-chip: new opportunities for analytical applications. Microfluid. Nanofluid. 1:22-40

Ginder JM, Davis LC (1994) Shear stresses in magnetorheological fluids: role of magnetic saturation. Appl. Phys. Lett. 65:3410-3412

Ginder JM, Davis LC, Elie LD (1996) Rheology of magnetorheological fluids: models and measurements. International Journal Modern Physics B 10:3293-3303

Haukanes B-I, Kvam C (1993) Application of magnetic beads in bioasays. Nature Biotechnology 11:60-63

Hayes MA, Polson NA, Garcia AA (2001) Active Control of Dynamic Supraparticle Structures in Microchannels. Langmuir 17:2866-2871

Hellmich W (2006) Einzelzellananlytik in Mikrofluidik-Systemen. PhD thesis, Bielefeld University

Jackson JD (1975) Classical electrodynamics, 2nd edition, Wiley, New York

Jackson MB (2006) Molecular and cellular biophysics. Oxford University Press, Oxford

Jäger S and Klapp SHL (2011) Pattern formation of dipolar colloids in rotating fields: layering and synchronization. Soft Matter 7:6606

Jäger S, Schmidle H, Klapp SHL (2012) Non-equilibrium condensation and coarsening of field-driven dipolar colloids. arXiv:1203.0858v1

Kalontarov M, Tolley MT, Lipson H, Erickson D (2009) Hydrodynamically driven docking of blocks for 3D fluidic assembly. Microfluid. Nanofluid. 9:551-558

Karle M, Wöhrle J, Miwa J, Paust N, Roth G, Zengerle R, von Stetten F (2011) Controlled counter-flow motion of magnetic bead chains rolling along microchannels. Microfluid. Nanofluid. 10:935-939

Korgel B, Fullam S, Conolly S, Fitzmaurice D (1998) Assembly and self-organization of silver nanocrystal superlattices: Ordered soft spheres. J. Phys. Chem. 102:8379

Kim YS, Park IH (2010) FE analysis of magnetic particle dynamics on fixed mesh with level set function. IEEE Trans. Magn. 46(8):3225-3228

Lacharme F, Vandevyver C, Gijs MAM (2009) Magnetic beads retention device for sandwich immunoassay: comparison of off-chip and on-chip antibody incubation. Microfluid. Nanofluid. 7:479–487

LaMer VK, Dinegar RH (1950) Theory, production and mechanism of formation of monodispersed hydrosols. J. Am. Chem. Soc. 72:4847-4854

Laroze D, Vargas P, Cortes C, Gutierrez G (2008) Dynamic of two interacting dipoles. J. Magn. Magn. Mat. 320:1440-1448

Leunissen ME, Vutukuri HR, van Blaaderen A (2009) Directing colloidal self-assembly with biaxial electric fields. Adv. Mater. 21:3116-3120

Love LJ, Jansen JF, McKnight TE, Roh Y, Phelps TJ, Yeary LW, Cunningham GT (2005) Ferrofluid field induced flow for microfluidic applications. IEEE Transactions on Mechatronics 10:68-76

Meijering E, Dzyubachyk O, Smal I (2012) Methods for cell and particle tracking. Methods in Enzymology 504:183-200

Melle S, Calderón OG, Rubio MA, Fuller GG (2003) Microstructure evolution in magnetorheological suspensions governed by Mason number. Phys. Rev. E 68:041503

Mørup S, Hansen MF, Frandsen C (2010) Magnetic interactions between nanoparticles. Beilstein J. Nanotechnol. 1:182-190

Moskowitz R, Rosensweig RE (1967) Nonmechanical torque-driven flow of a ferromagnetic fluid by an electromagnetic field. Appl. Phys. Lett. 11:301-303

Motte L, Courty A, Ngo AT, Lisiecki I, Pileni MP (2005) Self-organization of Inorganic Nanocrystals in Nanocrystals forming mesoscopic structures. Wiley-VCH Verlag, Weinheim

Ng J, Gitlin I, Stroock A, Whitesides GM (2002) Components for integrated poly(dimethylsiloxane) microfluidic systems. Electrophoresis 23(20):3461

Niarchos D (2003) Magnetic MEMS: key issues and some applications. Sensors Actuators A: Physical 109:166-173

Ohara PC, Leff DV, Heath JR, Gelbart WM (1995) Crystallization of opals from polydisperse nanoparticles. Phys. Rev. Lett. 75:3466

Østergaard S, Blankenstein G, Dirac H, Leistiko O (1999) A novel approach to the automation of clinical chemistry by controlled manipulation of magnetic particles. J. Magn. Magn. Mat. 194: 156-162

Ostwald W (1896) Lehrbuch der allgemeinen Chemie, vol.2 part I. Veit, Leipzig

Ovid'ko IA (2004) Interfacial defects in Nanostructures. Encycl. Nanosci. Nanotechnology 4:249-265 ISBN:9781588830012

Pamme N (2006) Magnetism and microfluidics. Lab Chip 6:24-38

Pamme N, Manz A (2003) On-chip free flow magnetophoresis: continous flow separation of magnetic particles and agglomerates. Lab Chip 3:187-192

Panhorst M, Kamp PB, Reiss G, Brückl H (2005) Sensitive bond-force measurements of ligand-receptor pairs with magnetic beads. Biosens. Bioelectron. 20(8):1685-1689

Petousis I, Homburg E, Derks R, Dietzel A (2007) Transient behavior of magnetic micro-bead chains rotating in a fluid by external fields. Lab Chip 7:1746–1751

Radoszkowicz L, Presiado I, Erez Y, Nachliel E, Huppert D, Gutman M (2011) Time-resolved emission of flavin adenine dinucleotide in water and water-methanol mixtures. Phys. Chem. Chem. Phys. 13:12058-12066

Rasband, W.S. (1997-2011), ImageJ, U. S. National Institutes of Health, Bethesda, Maryland, USA, http://imagej.nih.gov/ij/

Regtmeier A, Wittbracht F, Rempel T, Mill N, Peter M, Weddemann A, Mattay J, Hütten A (2012) Uniform growth of clusters of magnetic nanoparticles in a rotating magnetic field. J. Nanopart. Res. (*revision submitted*)

Riley EK, Lidell CM (2010) Confinement-cotrolled self assembly of colloids with simultaneous isotropic and anisotropic cross-section. Langmuir 26:11648-11656

Rosensweig RE (1996) "Negative Viscosity" in a magnetic fluid. Science 271:614-615

Sawetzki T, Rahmouni S, Bechinger C, Marr DWM (2008) In situ assembly of linked geometrically coupled microdevices. Proc. Natl. Acad. Sci. USA 105:20141

Shliomis MI, Morozov KI (1994) Negative viscosity of ferrofluid under alternating magnetic field. Phys. Fluids 6(8):2855-2861

Sudfeld D (2005) Hochauflösende Mikrostrukturanalyse von magnetischen $(Fe_{1-x}Co_x)_{1-y}Pt_y$ Nanopartikeln. PhD thesis, Bielefeld University

Sugimoto T (2001) Monodispersed particles. Elsevier, Amsterdam

Tang X, Conrad H (2000) An analytical model for magnetorheological fluids. J. Phys. D: Appl. Phys 33:3026-3032

Vuppu A, Garcia AA, Hayes MA (2003) Video microscopy of dynamically aggregated paramagnetic particle chains in an applied rotating magnetic field. Langmuir 19:8646-8653

Warnke CK (2003) Finite-element modeling of the separation of magnetic microparticles in a fluid. IEEE Trans. Magn. 39, 1771

Weddemann A (2009) A finite element analysis of a microfluidic lab-on-a-chip system employing magnetic carriers for biomedical applications. PhD thesis, Bielefeld University

Weddemann A, Wittbracht F, Auge A, Hütten A (2009) A hydrodynamic switch: microfluidic separation system for magnetic beads. Appl. Phys. Lett. 94:173501-1

Weddemann A, Wittbracht F, Eickenberg B, Hütten A (2010 a) Magnetic field induced assembly of highly ordered two-dimensional particle arrays. Langmuir 26:19225-19229

Weddemann A, Ennen I, Regtmeier A, Albon C, Wolff A, Eckstädt K, Mill N, Peter MKH, Mattay J, Plattner C, Sewald N, Hütten A (2010 b) Review and outlook: from single nanoparticles to self-assembled monolayers and granular GMR sensors. Beilstein J. Nanotechnol. 1:75-93

Weddemann A, Auge A, Kappe D, Wittbracht F, Hütten A (2010 c) Dynamic simulations of the dipolar driven demagnetization process of magnetic multi-core nanoparticles. J. Magn. Magn. Mat. 322(6):643-646

Weddemann A, Albon C, Auge A, Wittbracht F, Hedwig P, Rott K, Meißner D, Jutzi P, Hütten A (2010 d) How to design magneto-based total analysis systems for biomedical applications. Biosens. Bioelec. 26:1152-1162

Weddemann A, Wittbracht F, Auge A, Hütten A (2011) Particle flow control by induced dipolar interaction of superparamagnetic microbeads. Microfluid. Nanofluid. 10:459-463

Wittbracht F (2009) Manipulation magnetischer Beads in Mikrofluidiksystemen: Separation und Positionierung. Master thesis, Bielefeld University

Wittbracht F, Eickenberg B, Weddemann A, Hütten A (2011) Towards a programmable microfluidic valve: Formation dynamics of two-dimensional magnetic bead arrays in transient magnetic fields. J. Appl. Phys. 109:114503

Wittbracht F, Weddemann A, Eickenberg B, Zahn M, Hütten A (2012 a) Enhanced fluid mixing and separation of magnetic bead agglomerates based on dipolar interaction in rotating magnetic fields. Appl. Phys. Lett. 100:123507

Wittbracht F, Weddemann A, Eickenberg B, Hütten A (2012 b) On the direct employment of dipolar particle interaction in microfluidic systems. Microfluid. Nanofluid. DOI: 10.1007/s10404-012-0995-6 (*in press*)

Yeh CS, Chen KC (1997) A thermodynamic model for magnetorheological fluids. Continuum Mech. Thermodyn. 9:273-291

Zahn M, Pioch LL (1999) Ferrofluid flows in AC and travelling wave magnetic fields with effective positive, zero or negative dynamic viscosity. J. Magn. Magn. Mat. 201:144-148

Zborowski M, Liping S, Moore LR, Williams S, Chalmers JJ (1999) Continuous cell separation using novel magnetic quadrupole flow sorter. J. Magn. Magn. Mat. 194:224-230

Acknowledgments

At this point, I want to thank everybody, who contributed to this work. The projects presented in this thesis would not have been realized without the contributions of the following people:

First of all, I have to thank my supervisor Prof. Dr. Andreas Hütten. Throughout the last years he was always available for discussions, helped with ideas, resembled a constant source of motivation and gave me and the small microfluidics group in general the possibility and freedom to work on this interesting topic.

I thank Dr. Michael Schilling for introducing me to the topic of microfluidics on D2 and for his excellent training in the laboratory. Unfortunately, he left our workgroup and I was only able to benefit from his expertise for a couple of months. Nevertheless, he introduced me to most of the techniques described in the experimental section.

The next person in line to thank is Dr. Alexander Weddemann. He is not only responsible for all simulation results presented in this thesis, but he is also the person who led to most device ideas. Furthermore, I want to thank Alexander for proof reading this work. During the last five years it has been a great pleasure for me to work with this excellent theoretical physicist and mathematician, who has also a very good sense for experiments and knows that the Netherlands do not necessarily have to be in Europe.

I would like to thank Bernhard Eickenberg for his contributions to the experimental results in the framework of his Master's thesis. He is a very attentive experimentalist, originally trained in the Department of Chemistry, who now plays a vital role as a PhD candidate in the small microfluidics group on D2.

For the support throughout the years at Bielefeld University, for being such an excellent colleague and last but not least for proof reading this work, I want to thank Alexander Auge.

I thank Peter Hedwig for discussions, ideas and help with whatever electronics problem may have occurred and also for proof reading this work.

Thanks to all those, who worked in the offices D2-118 and D2-246 for their patience and for being there for discussions if necessary.

In particular, I want to thank Dr. Karsten Rott, Nadine Mill and Aggi Windmann for their kind help in context with almost all laboratory equipment (Karsten), questions concerning the chemistry lab (Nadine) and all sorts of administration issues (Aggi).

I thank all colleagues who worked on D2 throughout the years for the nice working atmosphere.

I thank my family for the continuous support and finally, I thank Katrin.